Washington University in St. Louis
Washington University Open Scholarship

Spring 5-15-2014

Engineered Plasmonic Nanostructures for Nanomedicine

Christopher Matthew Portz
Washington University in St. Louis

Follow this and additional works at: https://openscholarship.wustl.edu/eng_etds

Part of the Mechanical Engineering Commons

WASHINGTON UNIVERSITY IN ST. LOUIS
School of Engineering and Applied Science
Department of Mechanical Engineering and Material Science

Thesis Examination Committee:
Dr. Srikanth Singamaneni
Dr. Parag Banerjee
Dr. Jerry Morrissey

Engineered Plasmonic Nanostructures for Nanomedicine
by
Christopher Matthew Portz

Contents

List of Figures

Acknowledgments

I would first like to thank Professor Srikanth Singamaneni and Naveen Gandra for allowing me to assist in and carry out important experiments in the Soft Nanomaterials Laboratory at Washington University in St. Louis, as well as sharing their depth of knowledge in the field of nanofabrication.

Continuing, my expression of thanks goes to the many graduate students and distinguished faculty within my department who have offered their support and guidance through this process.

Christopher Matthew Portz

Washington University in St. Louis
May 2014

Dedicated to my parents and wife for their constant support.

ABSTRACT

Engineered Plasmonic Nanostructures for Nanomedicine Imaging, Sensing, and Therapy

Applications

By Christopher Matthew Portz

Master of Science in Mechanical Engineering

Washington University in St. Louis, 2014

Research Advisor: Dr. Srikanth Singamaneni

Metal nanostructures are emerging as an important class of materials for nanomedicine due to the unique combination of physical, chemical, and biological properties such as large absorption and scattering cross-section, high sensitivity to local dielectric environment, and enhanced electric field at the surface.   High sensitivity of plasmonic nanostructures and their assemblies to the changes in the refractive index of the surrounding medium allows them to serve as a sensitive nanotransducer for the detection of chemical and biochemical analytes., These nanostructures also serve as 'nanoheaters' for photothermal therapy due to the large absorption cross-section. Yet another important manifestation of enhanced electric field at the surface of plasmonic nanostructures is surface enhanced Raman scattering (SERS), which involves the dramatic enhancement of Raman scattering from molecules adsorbed on or in close proximity to nanostructured metal surface. SERS has garnered much attention owing to its potential applications in chemical and biological sensing, environmental monitoring, and bioimaging.   SERS is particularly attractive in molecular bioimaging owing to its (i) large multiplexing ability; (ii) excellent photostability compared to organic dyes; (iii) absence of interference from water (iv) high spatial resolution; and (v) use of bio inert materials such as gold. However, SERS based bioimaging remains a challenge due primarily to the lack of bright, easy-to-synthesize, stable and reproducible SERS probes.

Except for a few reports, most of the current SERS probe (i.e., contrast agents) designs so far involve individual plasmonic nanostructures uniformly appended with Raman reporters, which offer limited SERS enhancement and suffer from poor stability due to desorption or enzymatic degradation of the Raman reporters in physiological environment. In this context, we designed and developed a novel SERS probe design, which involves trapping Raman reporter molecules between two concentric nanostructured gold layers (i.e., gold core and shell). The novel SERS probe demonstrated here offers nearly 20 times brighter SERS intensity compared to existing SERS tags

based on individual gold nanostructures. Furthermore, so far most of the efforts have been limited to design and optimization of the plasmonic nanostructures to perform either imaging or targeted delivery. In this study, we explored two designs of an all-in-one plasmonic nanostructure, which can be tracked non-invasively using NIR light, externally triggered to release the drug and non-invasively monitor the cargo level in the carriers at different stages. The first design involved Janus nanostructures that are comprised of hollow (drug carrier) and solid (SERS tag) parts, which renders multifunctionality to the envisioned nanostructures. We choose SERS tags as optical label owing to their ultra-bright nature, large multiplexing ability, and more importantly, their photostability. A second design involved plasmonic nanorattles comprised of a bright SERS probe trapped in a porous gold shell. The SERS signal from nanorattles, comprised of two Raman reporters, was designed to report the state of the plasmonic nanostructure.

We extended the plasmonic engineering principles to fluorescence enhancement of NIR dyes that typically suffer from poor quantum yields. Specifically, the distance-dependent fluorescence enhancement of NIR dyes in proximity to gold nanostructures is explored using layer-by-layer assembled polymer multilayer as a dielectric spacer. We noted nearly three order magnitude enhancement in fluorescence signals under optimal conditions. The study lays the groundwork for the design and synthesis of extremely bright Raman and fluorescence probes based on optimal design of plasmonic nanostructures. The design principles established here can be extended to other Raman reporters and fluorescent dyes to achieve a suite of optical probes for highly sensitive, precise and accurate bioimaging.

Chapter 1
Introduction to Plasmonic Nanomedicine

1.1 Localized Surface Plasmon Resonance

Surface plasmon involves the collective coherent oscillation of the conductive electrons at the interface of a metal and dielectric material. A broad term, plasmonics involves the control of light at the nanoscale using surface plasmons, which encompasses such unique optical phenomena as highly localized enhancement of electromagnetic (EM) field at nanostructured metal surface, high sensitivity of the surface plasmon resonance to external medium, extraordinary transmission through sub-wavelength apertures in thin metal films, and sub-wavelength waveguiding in metal nanostructures. Plasmonics is gaining immense interest due to potential applications of the aforementioned phenomenon in nano-optical components for plasmonic circuits, fabrication of nanoscale structures, photovoltaics, and chemical/biological sensors.[1]

Figure 1 UV-Visible extinction (black), absorption (red), and scattering spectrum (blue) of Ag nanocrystals, illustrating the effect of shape on spectral characteristics: (a) sphere, (b) cube, (c) tetrahedron and (d) octahedron. Reprinted with permission from Xia et al. [4].
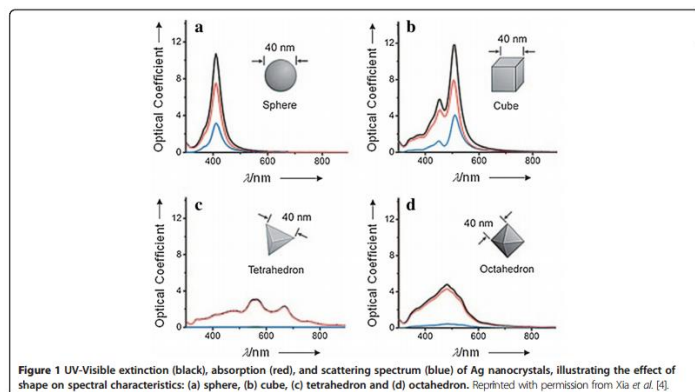
Figure 1.1 – UV-Visible extinction (black), absorption (red), and scattering (blue) of Ag nanoscrystals, illustrating the effect of shape on spectral characteristics: (a) sphere, (b) cube, (c) tetrahedron, and (d) octahedron.[2]

The time varying electric field of the electromagnetic radiation causes oscillation of conductive electrons in the nanoparticles. The resonance of such oscillation, termed localized surface plasmon resonance (LSPR), falls into the visible regime for noble metals such as gold, silver and copper. The LSPR of metal nanostructures is sensitive to numerous factors such as composition, size, shape, dielectric ambient, and proximity to other nanostructures via plasmon coupling. The sensitivity of LSPR to localized changes in

dielectric environment renders it an attractive transduction platform for chemical and biological sensing.
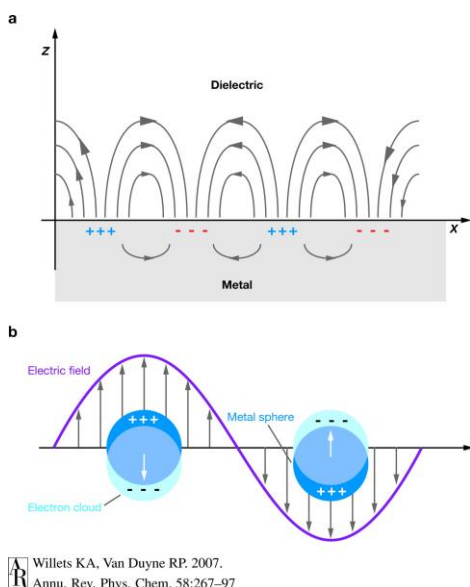
Willets KA, Van Duyne RP. 2007.
Annu. Rev. Phys. Chem. 58:267–97

Figure 1.2 – (a) a surface plasmon polariton and (b) a localized surface plasmon for metal nanospheres.[3]

The localized surface plasmon resonance of metal nanoparticles can be tuned based on size, geometry, and composition. Spherical nanoparticles are isotropic and will have a single LSPR peak, but can be tuned with size. Increase in nanoparticle size will red shift the LSPR peak, and conversely the smaller nanoparticles will exhibit a blue shifted peak in comparison. Growing subsequent shells around the spherical cores can grow spherical nanoparticles to larger sizes. Asymmetric growth continues the red shift trend as the size is increasing although not isotropically. Other geometries have more complex features on a UV-Vis spectrum. Nanorods are anisotropic and exhibit two peaks, the longitudinal LSPR and transverse LSPR. The transverse band is not very sensitive to the diameter and length of the nanorod; however, the longitudinal band is highly sensitive to the aspect ratio of the nanorods. The longitudinal band exhibits a red shift with an increase in aspect ratio. Other anisotropic nanostructures such as nanostars exhibit a broad peak, which is due to the large variation is topography of the structures. Although, less explored composition of the nanostructures also provides additional handles in tuning the LSPR of plasmonic nanostructures. In this study, we demonstrate compositionally asymmetric nanostructures using kinetic control in the seed-mediated growth of core-shell nanostructures.

1.2 Surface Enhanced Raman Scattering

Despite the rich molecular information provided by Raman spectroscopy, the technique was not considered to be a practical analytical tool (let alone detection tool) due to the extremely weak signal intensity of normal Raman scattering, a result of the extremely small scattering cross-section for most molecules except some special cases (e.g. resonance Raman scattering). Hence, for the longest period after its discovery, Raman scattering remained limited to "bulk" material investigations.

Surface enhanced Raman scattering (SERS) involves dramatic enhancement in the intensity of the Raman scattering from the analyte adsorbed on or in proximity to a rough (nanoscale) metal surface. Despite the initial controversy, at present there is consensus that the enhancement of the Raman signal originates from two distinct contributions, namely, electromagnetic enhancement and chemical enhancement with the former effect being several orders of magnitude higher than the later. When the excitation light is in resonance with the plasmon frequency of the metal nanoparticle, it radiates a characteristic dipolar radiation causing a characteristic spatial distribution in which certain areas show higher intensity, which is manifested as an electromagnetic enhancement. Analyte molecules subjected to this enhanced electromagnetic field exhibit a dramatic enhancement in Raman scattering. Electromagnetic enhancement critically depends on numerous factors such as distance between the metal nanostructures, size and shape (i.e. antenna effect) of the nanostructures, composition of the metal nanostructures, and the excitation wavelength with respect to the plasmon resonance of the metal nanostructures.

1.3 Plasmonics in Nanomedicine

One area, in particular, where plasmonics is expected to make an enormous impact is the field of life sciences with applications in high-contrast imaging, and non-invasive or minimally invasive diagnostics and therapeutics. Based on the sensitivity of the surface plasmon resonance to the dielectric ambient and the enhancement of EM field in proximity to metal nanostructures, two important classes of plasmonic biosensors are being actively investigated (see Figure 1.3).

Conventional SPR sensors rely on propagating surface plasmons at the interface of thin metal films and a dielectric medium. The sensitivity of the surface plasmon resonance (SPR) to the changes in the dielectric ambient is exploited in SPR based sensing, which is currently a well-established technique for biosensing and probing thermodynamic and kinetic aspects of biomolecular binding.[5,6] Although extremely sensitive, conventional SPR suffers from complexity in exciting the surface plasmons (requiring complex optical alignment or special substrates such as prisms) and more importantly lacks the spatial resolution to address single or few molecule events.
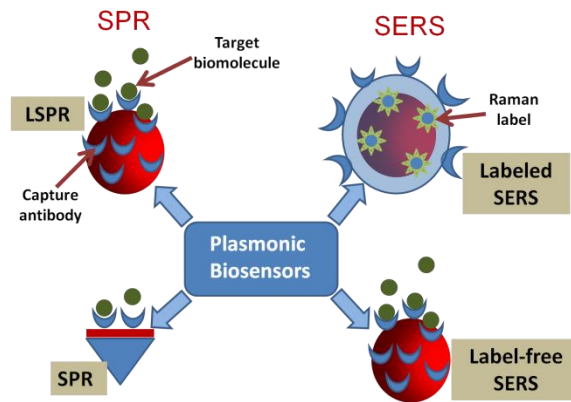
Figure 1.3 –There are two important classes of plasmonic biosensors: surface plasmon resonance biosensors and surface enhanced Raman scattering biosensors.

On the other hand, excitation of surface plasmons in metal nanostructures (significantly smaller than the wavelength of light) does not require a specialized setup, simplifying the operation and making them more appropriate for on-chip, point of care, and cost-effective diagnostics. The time varying electric field of the electromagnetic radiation causes oscillation of conductive electrons in the nanoparticles. The resonance of such oscillation, termed localized surface plasmon resonance (LSPR), falls into the visible regime for noble metals such as gold, silver and copper. LSPR of metal nanostructures is sensitive to numerous factors such as composition, size, shape, dielectric ambient, and proximity to other nanostructures (plasmon coupling).[7,8] The sensitivity of LSPR to localized changes in dielectric environment renders it an attractive transduction platform for chemical and biological sensing.[9,10,11,12,13] LSPR overcomes the above mentioned deficiencies of the

4

conventional SPR approach due to the simplicity of exciting surface plasmons in metal nanostructures and the ability to address the same analytes down to single nanostructures enabling high lateral resolution and single molecule detection.[14,15] One fundamental question that immediately arises is the sensitivity of LSPR sensors in comparison to the conventional SPR approach. In a recent study, Käll and co-workers have demonstrated that the sensitivity of LSPR and SPR are comparable from a biosensing standpoint.[16] Although SPR exhibited higher refractive index sensitivity and figure of merit (refractive index sensitivity/full width at half maximum of the SPR) compared to LSPR, much smaller decay length of the LSPR compared to the SPR imparts higher surface sensitivity to LSPR, thus making it equally sensitive in biosensing applications. In summary, LSPR offers distinct advantages compared to traditional SPR approach: (i) low bulk sensitivity (ii) simplicity in detection (iii) high spatial resolution down to single nanoparticle and (iv) facile integration with device platforms for developing point of care assays. These favorable traits form the rationale behind our choice of LSPR as a transduction platform for the present study.

SERS is being investigated for the fabrication of highly sensitive label free biosensors and as an imaging tool from a biomedical standpoint,. Biosensors based on SERS can be broadly classified into labeled and label-free approaches (see Figure 1.3). In the labeled approach, Raman marker (reporter molecules) and captured biomolecules are bound to metal nanostructures. Upon binding of this composite nanostructure to the target analyte, the Raman signal from the Raman marker is detected and quantified to estimate the analyte concentration. Apart from its application in in vitro biosensors, the labeled SERS approach has also been demonstrated to be valuable in imaging tumors by targeted accumulation of gold nanostructures. An alternate approach (label-free) involves binding of the analyte to the metal nanostructure functionalized with the captured biomolecule followed by the detection and quantification of the Raman scattering from the analyte itself. The inherently narrow Raman bands as opposed to broad fluorescence bands enable multiplexed detection of multiple analytes in a complex mixture. Both labeled and label-free approaches are being extensively investigated for the detection of a wide variety of biological species.

SERS is also being extensively investigated as a bioimaging modality, especially for intraoperative settings. SERS is particularly attractive in molecular bioimaging owing to its

(i) large multiplexing ability; (ii) excellent photostability compared to organic dyes; (iii) absence of interference from water (iv) high spatial resolution; and (v) use of bioinert materials such as gold. However, SERS based bioimaging remains a challenge due primarily to the lack of bright, easy-to-synthesize, stable and reproducible SERS probes. Except for a few reports, most of the current SERS probe (i.e., contrast agents) designs typically involve individual plasmonic nanostructures uniformly appended with Raman reporters, which offer limited SERS enhancement and suffer from poor stability due to desorption or enzymatic degradation of the Raman reporters in physiological environment. Extensive efforts have been dedicated to developing novel instrumentation and techniques that facilitate the deployment of SERS-based bioimaging in clinical settings and imaging of deep tissues. Intraoperative hand-held device is an excellent tool for a surgeon to identify tumor margins and satellite nodules during surgical procedures. Nie and co-workers have developed a hand-held spectroscopic device called SpectroPen that enables wavelength-resolved fluorescence and Raman measurements for in vivo and intraoperative SERS-based bioimaging applications.[17] A different line of efforts are focused on enhancing the depth of imaging. It is known that commonly employed backscattering geometry suffers from limited depth of penetration (few mm) even in NIR range due to highly diffusive nature of living tissue. An alternate method known as spatially offset Raman spectroscopy (SORS) involves spatially offsetting the collection of Raman scattered light from the excitation regions (i.e., laser incident regions), which enables the collection of diffuse component of scattered light as opposed to conventional ballistic and snake photons in backscattering geometry, thus significantly enhancing the depth of probing. Recently this method has been integrated with SERS resulting in spatially offset SERS (SESORS), which enables significantly deeper probing into mammalian tissue.[18] Multiplexed Raman signals emanating from SERS probes buried 25 mm deep inside a porcine tissue were successfully collected and analyzed by offsetting the excitation and collection by 180° i.e., transmission Raman spectroscopy, a special case of SORS. More recently, Gambhir and co-workers have integrated a fiber optic-based Raman spectrometer with a white light endoscope to perform Raman imaging of human colon.[19] In a different line of efforts, Bhatia and coworkers have demonstrated implantable NIR sources, which overcome the depth limitation associated with NIR light-based therapies.[20]

Multifunctional nanostructures that enable targeted and externally-triggered delivery of therapeutic agents along with non-invasive tracking and monitoring of the therapy process are a holy grail in nanomedicine. Different classes of nanomaterials including supramolecular assemblies, polymer capsules, and hollow metal nanostructures are extensively investigated for such applications.[21,22,23,24,25,26,27,28,29,30,31,32,33] However, in most of these cases, it is difficult to track the drug carrying vehicle and to monitor the therapeutic response in a noninvasive- or minimally-invasive manner. Even in the case of nanocarriers that comprise of a fluorescent tag, photobleaching of the dyes severely limits the duration over which the carrier can be tracked. Additionally, spontaneous release of drugs based on biological or intrinsic factors typically results in inadvertent deposition on normal tissue, leading to deleterious side effects. Therefore, the design and fabrication of multifunctional nanostructures, which can not only carry and release payload with an external trigger but also be amenable to non-invasive tracking of the carriers and the extent of drug release over long periods, is critical to enhance the efficacy of locoregional chemotherapy. In this study we have designed and demonstrated a novel class of multifunctional plasmonic nanostructures for image-guided therapies.

Chapter 2
Bimetallic Janus Nanostructures via Programmed Shell Growth

2.1 Abstract

We report the synthesis of compositionally asymmetric, core-Janus shell plasmonic nanostructures comprised of Au and Ag. Kinetic control was employed to achieve asymmetric shell growth on Au nanoparticles acting as cores. Subsequent differential surface functionalization of the nanostructures enabled programmed shell growth resulting in core-Janus shell nanostructures. UV Vis extinction spectra reveal that the localized surface plasmon resonance of the nanostructures depends on composition and distribution of the components, providing additional handles for tuning the optical properties of metal nanostructures. The core-Janus shell nanostructures demonstrated here are highly Raman-active making them attractive candidates for Raman-based biosensing and bioimaging applications.

2.2 Introduction

We have produced a bimetallic nanostructure, which is asymmetric. These are called gold and silver Janus nanostructures. The term 'Janus' structure comes from the Greek god of doorways, Janus. This Greek god had two opposite facing faces, which represent looking to the future as well as the past. The nanoparticles are half silver and half gold, each with its own hemisphere. The mechanism for this type of growth is highly dependent on the kinetics of the reaction.

Localized surface plasmon resonance (LSPR), which involves the collective oscillation of dielectrically confined conduction electrons in metal or heavily-doped semiconducting nanostructures, enables the confinement of light to regions with sub-wavelength dimensions. Optical properties of metal nanostructures strongly depend on the size, shape, composition, dielectric environment, and inter-particle coupling of metal nanoparticles.[34-38] Shape and composition of metal nanostructures are two important handles that provide large tunability in the optical properties of metal nanostructures.[39, 40] Last decade has witnessed tremendous

progress in the synthesis of size- and shape-controlled metal nanostructures using, for example, seed-mediated and polyol methods.[34, 36] This progress in chemical synthesis of optically-tunable metal nanostructures has reflected in remarkable advancement in the fundamental understanding of their complex optical properties and numerous applications from biomedicine to photovoltaics.[41-43]

There has been a growing interest in composition-controlled bimetallic nanostructures owing to the synergistic properties of the constituent materials.[44] The optical properties of such bimetallic nanostructures depend not only on the composition but also to the relative distribution of the components within the nanostructures.[45] For example, gold and silver exhibit distinct and strong plasmon bands and together they cover the entire range of visible and parts of near infrared spectrum. Uniform Au-Ag alloy, core-shell, and asymmetric nanostructures have been synthesized using different reaction conditions.[39, 45, 46] Recently, it has been demonstrated that by controlling the kinetics of seed-mediated growth, site-selective growth of Ag and Au on Pd seeds can be achieved.[47] In particular, rate of addition of the precursor, capping agent, reductant, and reaction temperature play a critical role in controlling the growth of Ag and Au on Pd seeds. However, bimetallic Janus shell nanostructures comprised of Au and Ag have never been reported in the past. These kinds of precisely engineered bimetallic nanoparticles have several advantages in sensing, catalysis and photovoltaic applications due to their synergistic optical and catalytic properties.[42,45,46,48,49]
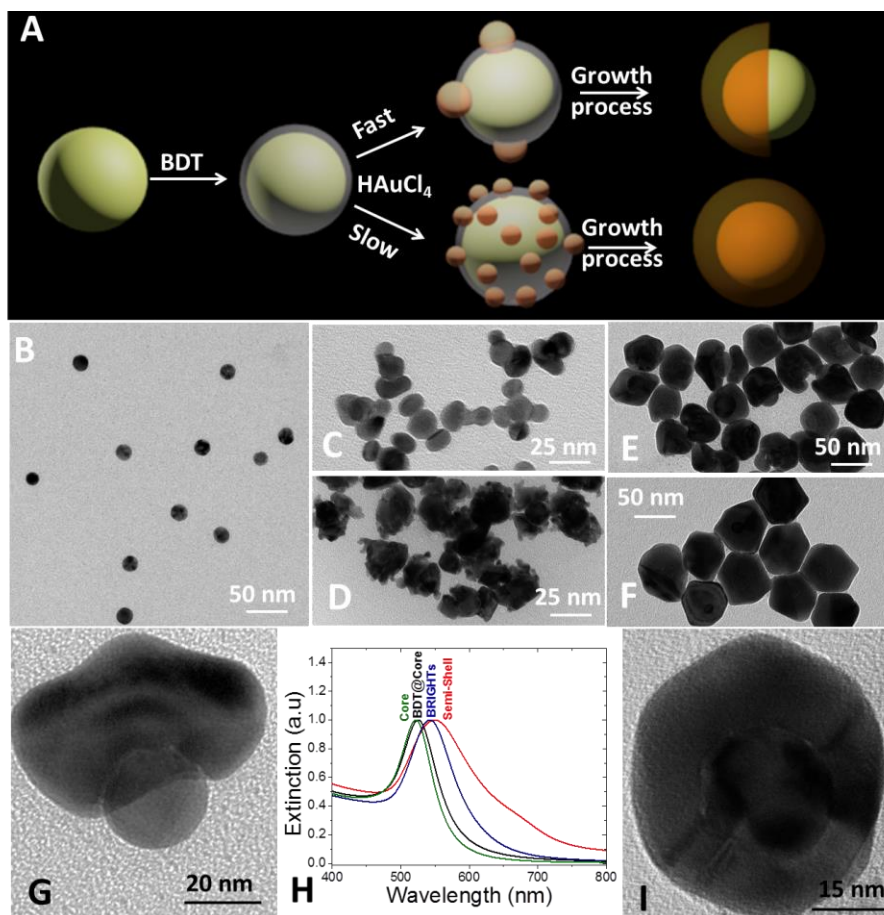
Figure 2.1 - Kinetically-controlled formation of Au core-semishell nanostructures. (A) A Schematic illustrating the mechanism of kinetically-controlled formation of core-semishell nanostructures. TEM images of (B) 20 nm Au nanoparticles, which were used as cores to synthesize core-semishell nanostructures after ligand exchange with BDT. (C-D) core-shell structures at intermediate stages of shell growth for both fast (C) and slow (D) reaction rates. (E) core-semishell and (F) core-shell Au nanostructures obtained by fast and slow growth rate of Au shell on Au cores, respectively. High-resolution TEM images of (G) core-semishell and (I) core-shell Au nanostructures described above. (H) Extinction spectra of Au cores, BDT-modified cores, core-shell (BRIGHTs), and core-semishell nanostructures. (Note: reaction conditions for fast and slow kinetics are included in materials and methods in supporting information)

Here, to the best of our knowledge, for the first time we report the synthesis of Au/Ag bimetallic Janus shell nanostructures. Bimetallic Janus shell nanostructures are realized in three steps: (i) synthesis and surface modification of 20 nm spherical gold nanoparticles, which serve as seed for bimetallic nanostructures; (ii) kinetically-controlled formation of Au semishell on the template nanoparticles; and (iii) differential surface modification of core-semishell structures for programmed silver growth to form Janus shell (Au-Ag) nanostructures (Figure 2.1 A, 2.2 A). We also demonstrate the intense SERS activity of such

10

nanostructures, which makes them ideal candidates as probes in SERS based bioimaging, biosensing and anti-counterfeit applications.

2.3 Synthesis of Bimetallic Nanostructures

The first step towards the synthesis of plasmonic nanostructures with asymmetric composition involves the synthesis of nanostructures with asymmetric core-shell structure. Figure 2.1 A illustrates the synthetic approach for the formation of Au core-semishell nanostructures. We employ kinetic-control for the growth of the semishell on the cores. Specifically, Au nanoparticles of 20 nm diameter capped with cetyltrimenthylammonium chloride (CTAC) were employed as cores (Figure 2.1B). The ligand on the Au nanoparticles was exchanged with 1,4-benzenedithiol, which is known to bind to Au through cleavage of -SH bond. The ligand exchange resulted in a nearly 3 nm red-shift in the LSPR wavelength of the Au cores (Figure 2.1H), which indicates the formation of a dense 1,4-Benzenedithiol (BDT) layer on the cores. A shell of desired thickness and morphology is grown by adding gold precursor ($HAuCl_4$), reductant (ascorbic acid), and surfactant (CTAC) to stabilize the core-shell structures. The morphology of the Au shell on cores can be kinetically controlled during shell nucleation and growth processes. The kinetics of the shell growth reaction was adjusted by varying the concentration of ascorbic acid in growth solution. Higher amount of ascorbic acid in the growth solution resulted in faster shell growth rate and in turn resulted in the formation of two to four discrete nucleation sites on BDT-modified cores (Figure 2.1C). These nuclei tend to grow and form a semishell (50-70%) on the surface of the core (Figure 2.1E). On the other hand, slow growth rate resulted in a rough but uniform shell possibly through multiple nucleation events on the surface of the BDT-modified cores (Figure 2.1D). Growth of such nuclei resulted in a uniform dodecahedral core-shell nanostructures (Figure 2.1F). We have previously demonstrated the high Raman intensity of such uniform core-shell nanostructures (as we called them BRIGHTs) and their application in SERS-based bioimaging.[41]   The UV/vis extinction spectra of the nanostructures demonstrate a significant red-shift in the LSPR wavelength of the core-shell nanostructures in agreement with our previous report.[41] Interestingly, the core-semishell structures exhibit a broad shoulder at higher wavelengths (λ=600-730 nm), which corresponds to the coupling

between the core and asymmetric semishell in agreement with previous reports involving such core-semishell structures.[50]
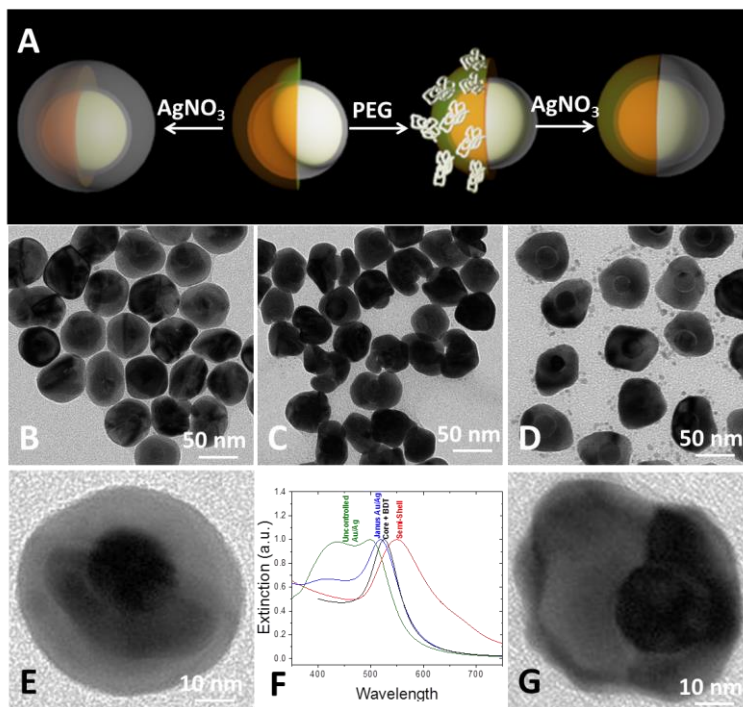

Figure 2.2 - Programmed shell growth using differential surface functionalization for realizing Janus bimetallic nanostructures. (A) Schematic representation of differential surface functionalization for programmed shell growth. TEM images of Au core-semishell nanostructures (C), Bimetallic Au/Ag core/shell nanostructures (B,E), and Bimetallic core-Janus shell nanostructures (D,G). (F) Extinction spectra of various nanostructures described above.

The core-semishell nanostructures are then employed as templates to synthesize bimetallic Janus nanostructures. Bimetallic Janus nanostructures are synthesized by selectively growing silver on the exposed regions of the core of core-semishell nanostructures (Figure 2.2A). To achieve the preferential growth of silver on the exposed regions of the core, the shell surface of the core-semishell structures was passivated with thiol-terminated poly(ethylene glycol) (SH-PEG). Addition of SH-PEG to core-semishell nanostructures resulted in the exchange of CTAC ligand on the semishell surface with SH-PEG, while the exposed regions of BDT-modified core remain intact. Subsequent addition of silver precursor (AgNO$_3$) resulted in the formation of a silver shell in the exposed regions, resulting in bimetallic core-Janus shell nanostructures (Figure 2.2 D). Higher resolution TEM image clearly demonstrates the Janus nanostructures with asymmetric composition (Figure 2.2G). Addition of silver precursor to

core-semishell structures without surface passivation step resulted in uniform silver shell on the entire core-semishell structure (Figure 2.2B, E). Clearly, differential surface functionalization is important to induce the growth of silver at desired locations on core-semishell structures and yield bimetallic core-Janus shell nanostructures. As mentioned above, the optical properties of bimetallic metal nanostructures depend on composition and distribution of the components. Extinction spectra of core-Janus shell nanostructures exhibited two bands corresponding to LSPR of Au (530 nm) and Ag (420 nm) with the LSPR band corresponding to Au significantly stronger than Ag owing to the small amount Ag (semishell) compared to Au (core+semishell). On other hand, core-semishell structures with uniform growth of Ag over the entire structure exhibited stronger LSPR band corresponding to Ag.
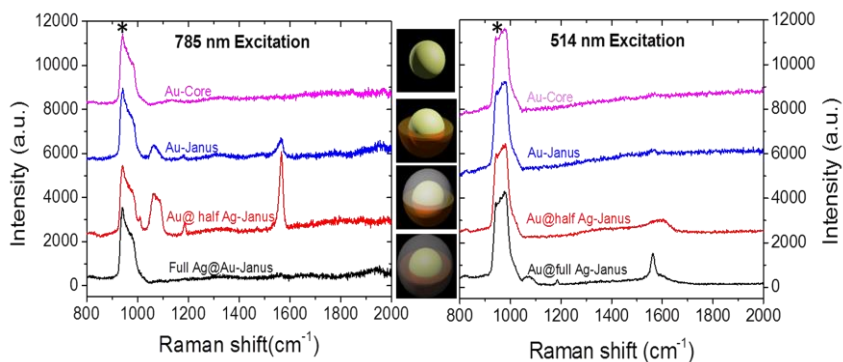
Figure 2.3 - Surface enhanced Raman scattering spectra of cores, core-semishells, bimetallic Au/Ag core/shells, and bimetallic core-Janus shell nanostructures obtained at both 785 and 514 nm of laser excitation sources. The band indicated with asterisk (*) in the spectrum from cores corresponds to the Raman band from the silicon substrate.

2.4 SERS Performance

Such core-shell and core-Janus shell plasmonic nanostructures with Raman-active molecules trapped between core and shell are extremely attractive as bright SERS tags.[46, 50] In fact, we have recently demonstrated that the Raman scattering from reporters (BDT) trapped between core and shell of a gold nanostructure is dramatically enhanced.[41] The SERS enhancement factor of such core-shell nanostructures is $\sim 2 \times 10^{11}$, making them ultra-bright nanostructures for bioimaging applications. SERS spectra obtained from various nanostructures using two excitation sources (514 and 785 nm) is shown in Figure 2.3. As expected, we did not observe any detectable Raman signal corresponding to BDT from

BDT-modified cores. Core-semishell nanostructures exhibited small but finite (955 cps) Raman signal with 785 nm excitation but no discernible Raman signal was observed using 514 nm excitation. This is possibly due to the plasmon resonance mismatch with excitation wavelength. Unlike core-semishell, core-shell structures showed reasonable signal intensity (1203 cps) under 514 nm excitation due to strongly match between plasmon resonance and excitation wavelength. On the other hand, core-Janus shell nanostructures exhibited the highest Raman intensity (3525 cps) among all these nanostructures with 785 nm excitation. Such strong Raman signal corresponds to plasmon coupling between the core and Janus shell, which results in enhanced EM field within the tiny gap between the core and shell, thus resulting in large SERS enhancement.[51]

Chapter 3
Multifunctional Nanorattles for Spectrum Guided Locoregional Therapy

3.1 Abstract

We demonstrate that a combination of photothermal ablation of the plasmonic nanorattles and triggered release of chemotherapeutic drug from the nanorattles can induce locoregional death of cancer cells in vitro. The completion of therapy process is indicated by a "Raman signal flip" between the two reporters of the SERS probe. Simple yet powerful approach to non-invasively monitor the therapy process serves as a new tool for precise control over the therapy process using plasmonic nanostructures.

3.2 Introduction

Nanotechnology holds great promise to achieve revolutionary advances in virtually all aspects of medicine including in vitro diagnostics, bioimaging, targeted, and externally-triggered therapy, image-guided surgery, and regenerative medicine. Multifunctional nanostructures that enable targeted and externally-triggered delivery of therapeutic agents along with non-invasive tracking and monitoring of the therapy process are a holy grail in nanomedicine.[52] Different classes of nanomaterials including supramolecular assemblies, polymer capsules, and hollow metal nanostructures are being extensively investigated for such applications.[53] However, in most of these cases, it is difficult to track the drug carrying nanovehicles over a long period to monitor the therapy process and therapeutic response non-invasively. Therefore, the design and fabrication of multifunctional nanostructures, which not only carry and release payload with an external trigger but are also amenable to non-invasive tracking of their location, extent of drug release, and progress of the therapy over long periods, is critical to enhance the efficacy of locoregional cancer therapy. In the last few years there have been significant efforts to employ hollow plasmonic nanostructures as drug carriers.[52b, 54] In particular, Xia and co-workers have demonstrated that chemotherapeutic drug can be encapsulated and released from gold nanocages using external trigger such as near infrared (NIR) laser or high-intensity focused ultrasound.[54b] A

15

temperature responsive polymer or phase change material is employed as a 'gate keeper' to contain or release the drug.[55]

We design and demonstrate multifunctional plasmonic nanorattles as nanocarriers to deliver therapeutics and to non-invasively monitor the therapy process. Plasmonic nanorattles are comprised of a surface enhanced Raman scattering (SERS) probe trapped in a porous gold shell. The SERS probe employed here is an upgraded version of the recently introduced SERS probe known as bilayered Raman-intense gold nanostructures with hidden tags (BRIGHTs).[56] Unlike BRIGHTs, which are comprised of one Raman reporter (1,4-benzenethiol (BDT)) trapped between Au core and shell, nanorattles are comprised of two Raman reporters. The two reporters (BDT and naphthalenethiol (NT)) molecules are precisely placed at distinct locations in the nanorattle. The SERS response of the nanorattles is governed by the morphological state of these nanostructures, which is used to monitor the therapy process. Irradiation with a NIR laser causes fragmentation of the outer shell of nanorattles and release of the drug encapsulated within. The fragmentation of the nanorattles is also associated with a dramatic switch in the SERS signal between the two reporters (BDT and NT) indicating the drug release. To the best of our knowledge, this is the first report describing multifunctional nanostructures which enable targeted delivery of payload with simultaneous monitoring of the payload release and the therapy process using SERS.
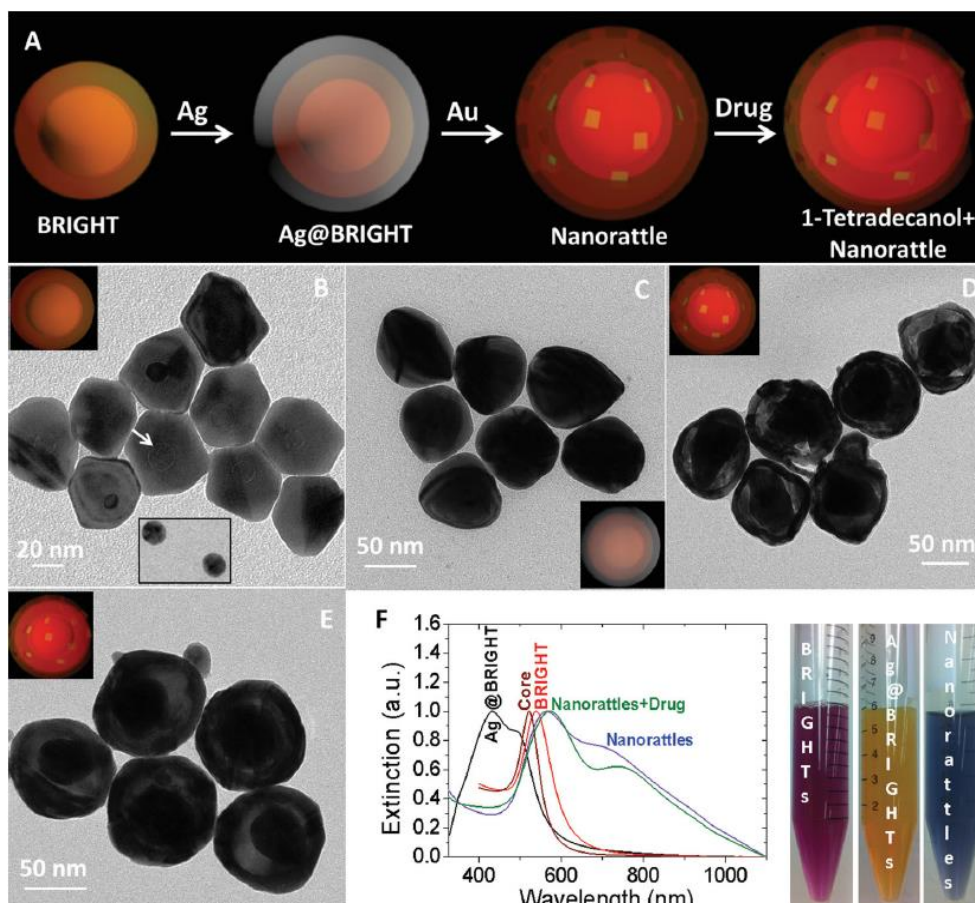
Figure 3.1 - Synthesis and drug loading into multifunctional nanorattles. A) Schematic representation of the synthesis of plasmonic nanorattles using BRIGHTs as cores. **B)** Transmission electron microscopy (TEM) image of BRIGHTs. Lower inset: TEM image of the core Au nanoparticles. **C)** TEM image of Ag@BRIGHT nanostructures, which shows ∼ 20 nm thick silver shell on BRIGHTs. **D)** TEM image of nanorattles revealing BRIGHT trapped in a porous Au shell. **E)** TEM image of drug-loaded nanorattles, which preserved their rattle structure during the drug loading process. Insets in (B–E): Corresponding schematic representation in (A). **F)** UV-vis extinction spectra of all the nanostructures mentioned above, depicting the evolution of the optical properties of Au nanorattles. Photographs of solutions of BRIGHTs, Ag@BRIGHTs, and nanorattles in Falcon centrifuge tubes.

3.3 Synthesis of Multifunctional Nanorattles

Various steps involved in the synthesis of multifunctional nanorattles are illustrated in Figure 3.1A. Synthesis of the multifunctional Au nanorattles starts with the synthesis of BRIGHTs as described previously,[56a] followed by chemisorption of second Raman reporter (NT) on the surface of these nanostructures. Briefly, BRIGHTs are comprised of BDT (employed as Raman reporters) trapped between Au core (20 nm diameter) and Au shell (25 nm thickness) (Figure 3.1B). Subsequently, a thin shell of Ag (∼20 nm) is grown on the surface of NT-modified BRIGHTs (Figure 3.1C). Galvanic replacement reaction is employed to convert

17

the Ag shell into a porous gold shell with BRIGHTs trapped inside (Figure 3.1D).[57] It is known that galvanic replacement of Ag nanostructures results in the formation of porous and hollow gold nanostructures, which have been employed as drug delivery agents.[54a,54c] The space between BRIGHT and outer shell is filled with a mixture of biocompatible phase change material (1-tetradecanol) and a chemotherapeutic drug (doxorubicin (Dox)) (Figure 3.1E). 1-Tetradecanol, which is known to exhibit a phase change from solid to liquid at around 39°C[55], serves as a gate keeper to contain or release drug from porous plasmonic nanostructures with external trigger such as light or ultrasound. [52b, 54b]

UV-vis extinction spectra reflect the changes in structure and composition of the nanostructures at various stages of synthesis (Figure 3.1F). BRIGHTs exhibit a LSPR band centered at 535 nm that is red-shifted and slightly broader compared to that of the Au nanoparticles employed as cores. Formation of a thin Ag shell on the BRIGHTs results in a new band at lower wavelength (410 nm) associated with Ag and ~46 nm blue shift in the LSPR wavelength of BRIGHTs. Following the galvanic replacement reaction, LSPR corresponding to Ag at lower wavelength completely disappeared with a concomitant emergence of a higher wavelength LSPR band (800 nm), which appears as a shoulder to slightly red-shifted BRIGHT's LSPR band at 550 nm. The red-shift in the BRIGHTs band is possibly due to the plasmonic coupling between the BRIGHT and the porous gold shell. The higher wavelength band, similar to that observed in Au nanocages obtained by using Ag nanocubes as templates, can be easily tuned by controlling the amount of gold salt added in the galvanic replacement reaction (Figure S3 Appendix C). In the present study, we employed 785 nm laser as the excitation source for obtaining SERS spectrum and 808 nm laser for photothermally heating the nanorattles. Thus, plasmonic nanorattles with LSPR wavelength at ~800 nm are ideal for both of these purposes.

3.4 SERS Performance

Now we turn our attention to SERS properties of the nanorattles. The nanorattles are comprised of two Raman reporters, namely, BDT and NT, located at two distinct locations as shown in Figure 3.2. BRIGHTs exhibit strong Raman scattering corresponding to BDT[56a] with 785nm excitation (Figure 3.2), which is trapped in between the core and shell of the BRIGHT structure. On the other hand, SERS signal from nanorattle corresponds to NT Raman bands (1378 cm^{-1} band corresponding to the ring stretch mode clearly distinguishes NT from BDT as shown in Figure 3.2[58], which is adsorbed on the surface of BRIGHTs. This is possibly due to the electromagnetic (EM) coupling between the porous Au shell and BRIGHT, which causes the NT molecules to reside at EM hot spots, thus dramatically enhancing their Raman scattering. These binary SERS-active nanostructures can be employed for probing the therapy process as will be demonstrated below. Briefly, laser ablation of nanorattles leads to rupture of the porous shell (TEM images in Figure S12 Appendix C), which in turn results in a "Raman signal flip" from NT to BDT. Complete flip in the SERS signal from NT to BDT indicates the rupture of the nanorattles and the completion of combination therapy by hyperthermia and release of chemotherapeutic drug.
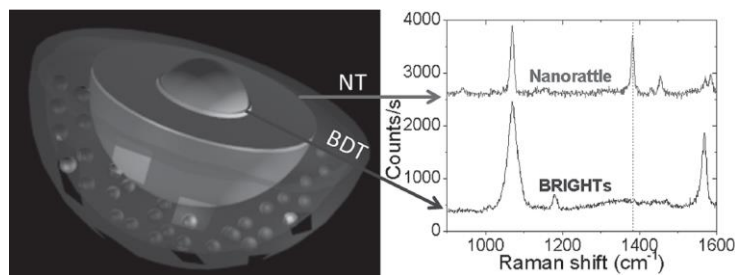

Figure 3.2 - Schematic depicting the location of BDT and 1-naphthalenethiol in the multifunctional nanorattle. SERS spectra corresponding to BRIGHTs and nanorattles are also depicted, which are dominated by BDT and NT signals, respectively.

3.5 Nanorattle Drug Delivery System

We demonstrate externally-triggered therapeutic efficiency of the nanorattles in vitro using epithelial breast cancer cells (SKBR3). Methylthiazolyldiphenyl-tetrazolium bromide (MTT) assay was employed to probe the viability of SKBR3 cells incubated with various concentrations of nanorattles. Up to a concentration of 5 nM of nanorattles or nanorattles loaded with tetradecanol, the cell viability was found to be higher than 90% (Figure 3.3). The

viability of cells incubated with 5 nM of tetradecanol-loaded nanorattles was found to be higher than 90% even with 808 nm laser irradiation (63.5 mW/cm^2 for 30 sec) indicating that the photothermal heating of the nanorattles at this laser power is insufficient to induce significant cell death (Figure 3.3). However, upon an increase of the laser power to 254mW/cm^2, the cell viability dropped to below 25%, due to the photothermal heating of the nanorattles (Figure S11 Appendix C). These results provide guidelines for the rational choice of laser power density to either cause or avoid photothermal destruction of cancer cells. Fluorescence microscopy was employed to probe the triggered release of Dox from the nanorattles in vitro. Dox is known to exhibit a moderately strong fluorescence emission at around 600 nm, which could be employed to monitor the release and distribution of the same drug[59]. SKBR3 cells were incubated with Dox-loaded nanorattles in serum-free
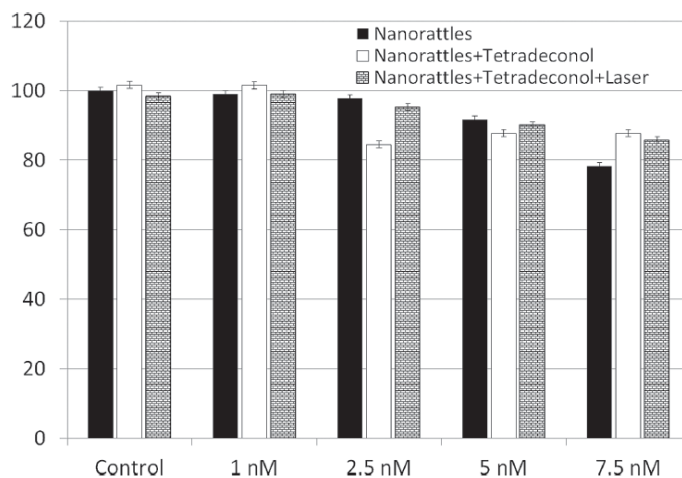

Figure 3.3 - Viability of epithelial breast cancer cells (SKBR3) in the presence of nanorattles, nanorattles loaded with tetradecanol, and nanorattles loaded with tetradecanol with laser exposure as determined by MTT assay.

medium for 2 hr at 37°C allowing passive internalization of the nanorattles.[60] Subsequently, the serum-free medium was replaced with complete medium and the cells were exposed to 808 nm laser for 30 sec at 63.5 mW/cm^2 power density. Fluorescence images of laser-treated cells were collected at 0, 30, 60, 120 min after laser irradiation was observed at 30 min (Figure 3.4). Although laser irradiation causes the release of Dox from nanorattles, the absence of fluorescence is due to the close proximity of Dox to gold nanostructures, which quenches the fluorescence in a non-radiative manner. However, at 60 min, a weak fluorescence signal was observed, which indicates the release and diffusion of Dox away from the nanorattles. Finally, at 120 min, strong red fluorescence was observed, which indicates the successful externally triggered-release of Dox from nanorattles. On the other hand, without laser irradiation, no noticeable release of Dox was observed indicating the
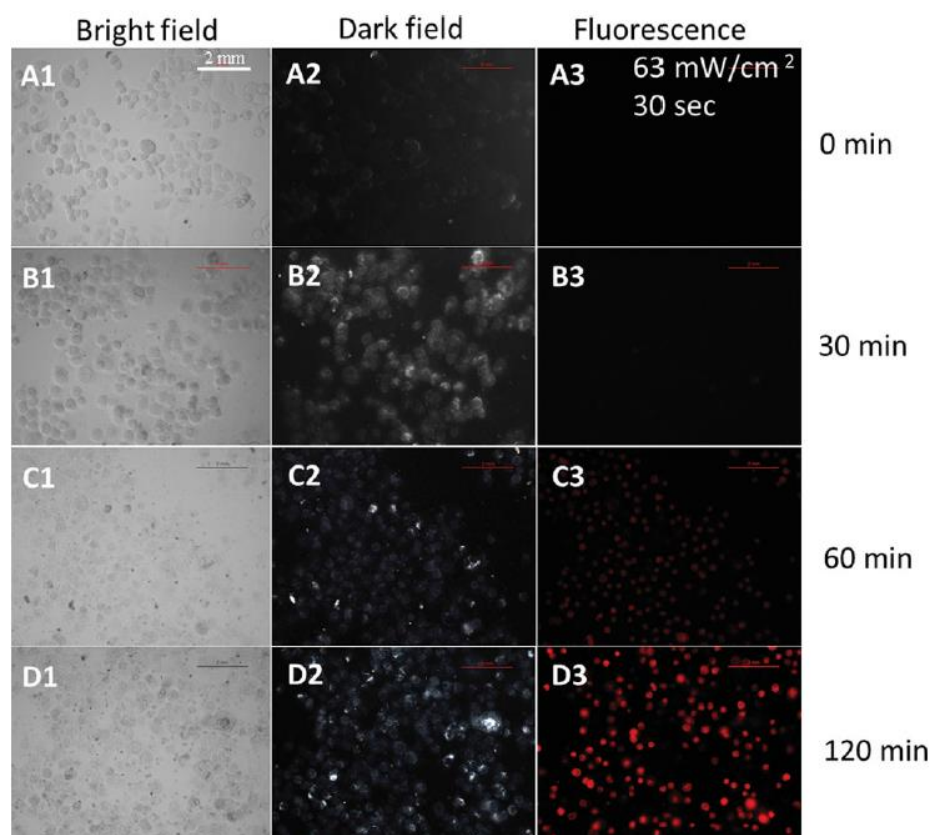

Figure 3.4 - Dox release studies upon laser exposure. Passively targeted SKBR3 cells are subjected to laser irradiation to follow the Dox release over a period of 120 min. The microscopy images in columns 1, 2, and 3 are bright field, dark field, and fluorescence images of SKBR3 cells, respectively. The microscopy images in rows A, B, C, D are images collected at 0, 30, 60, 120 min, respectively, after laser exposure. The fluorescence images in (A3–D3) clearly depict the Dox release (red fluorescence) 120 min after laser exposure.

21

absence of leakage or untriggered release of Dox (Figure S13 Appendix C).

Next, we investigate the therapeutic properties of nanorattles and Dox-loaded nanorattles with and without laser irradiation using commercially available live/dead viability kit (green color for live and red for dead) as shown in Figure 3.5. The cells in row B&C and rows D&E are incubated with nanorattles and Dox-nanorattles, respectively, for 2 hrs. Images in rows A, C, and E correspond to cells that were irradiated with 808 nm laser at a power density of 63.5 mW/cm^2 for 30 sec. The fluorescence images were collected after exposing the cells to live/dead staining solution for 30 min. The control cells after laser exposure exhibit bright green fluorescence, which corresponds to live cells and indicates that the laser power density employed here does not cause any cell death (Figure 3.5A3). Dark-field images of the cells incubated with nanorattles exhibit perceivable light scattering from the plasmonic nanostructures, confirming the passive uptake of the nanorattles by SKBR3 cells (Figure 3.5B2-E2). Uptake of the unfilled nanorattles itself does not cause any significant cell death as deduced from the strong green fluorescence from the cells and absence of any red fluorescence (Figure 3.5B3, 4). Similarly, laser irradiation of cells incubated with unfilled nanorattles did not cause any significant cell death (Figure 3.5C3, 4). On the other hand, uptake of Dox-loaded nanorattles results in observable change in cell morphology both with and without laser irradiation. In the case of unexposed cells (Figure 3.5D1-4), no strong staining of either green or red was observed, which indicates unhealthy state of cells. Laser irradiation of the cells with internalized Dox-loaded nanorattles resulted in severe cell death as indicated by the strong red fluorescence (Figure 3.5E4). These results clearly demonstrate that cell death is much faster and effective when incubated with drug-loaded nanorattles and irradiated with laser compared to all other cases.
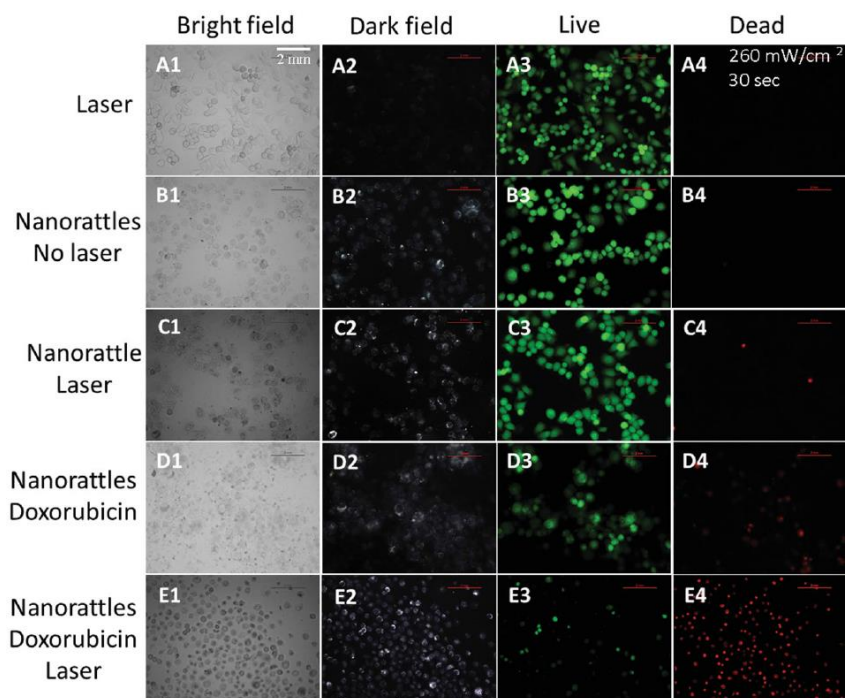
Figure 3.5 - Live/dead cell monitoring of SKBR3 cells. Columns 1, 2, 3, and 4 are bright field, dark field, green fluorescence (live), and red fluorescence (dead) microscopy images, respectively. Rows A, B, C, D, and E are only laser, only nanorattles, nanorattles + laser, nanorattles + Dox, and nanorattles + Dox + laser, respectively. All images collected after 60 min of incubation with ethidium bromide live/dead staining reagent. Cells treated with laser, nanorattles, and nanorattles + laser show a bright green fluorescence (A3–C3), which is an indication that the cells are alive. Cells treated with Dox-loaded nanorattles exhibit neither red nor green fluorescence, which is an indication of an unhealthy state of cells, possibly due to trace amounts of Dox released from the nanorattles. However, for the cells treated with laser light in the presence of Dox-loaded nanorattles, most of the cells are found to be dead (strong red fluorescence) as a result of the combination of chemotherapy and photothermal therapy.

MTT assay was employed to quantify the viability of SKBR3 cells incubated with Dox-loaded nanorattles with and without laser irradiation to further evaluate the effectiveness of therapy using plasmonic nanorattles. The viability of the cells was monitored at 4, 12 and 24 hours after 808 nm laser irradiation of the cells at a power density of 63.5 mW/cm^2 for 30 sec. Our studies show that laser irradiation of cells incubated with drug-loaded nanorattles results in significant cell death (with cell viability below 30%) at every measured time point shown by brick patterned bars in Figure 3.6. On the other hand, untreated cells (i.e., without laser irradiation) for the same time periods show significantly higher viability. For example, after 4 hrs, we observed a cell viability of ~90% for untreated cells whereas as the same drops to ~25% for laser-irradiated cells. These results demonstrate the rapid response of cells to laser irradiation suggesting that the combination therapy works much faster compared to individual therapies. These results are also consistent with the drug release

23

studies discussed above (Figure 3. and Figure S9 Appendix C). Significant cell death over a period of 24 hrs even in the case of untreated cells is possibly due to the trace amount of Dox that is released from the nanorattles over this long period of time.
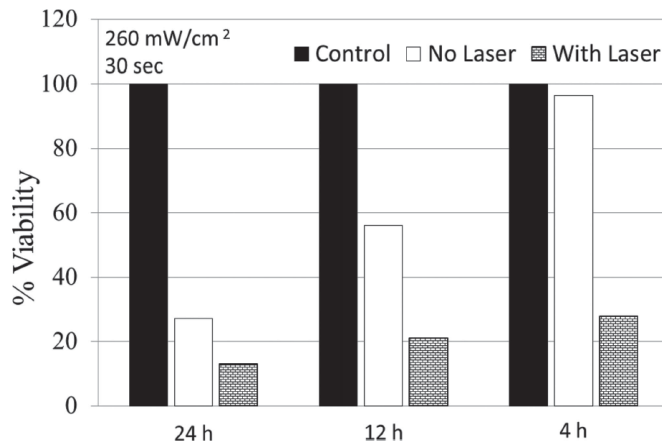

Figure 3.6 - Viability of SKBR3 cells at different time points (24, 12, and 4 h) with and without laser exposure in the presence of nanorattles loaded with 1-tetradecanol and Dox.

3.6 Tracking of Therapy Progress

As mentioned earlier, nanorattles enable one to follow the therapy process owing to the two Raman reporters incorporated into these plasmonic nanostructures. In particular, SERS signals from the nanorattles switch from NT to BDT depending on the structural state of
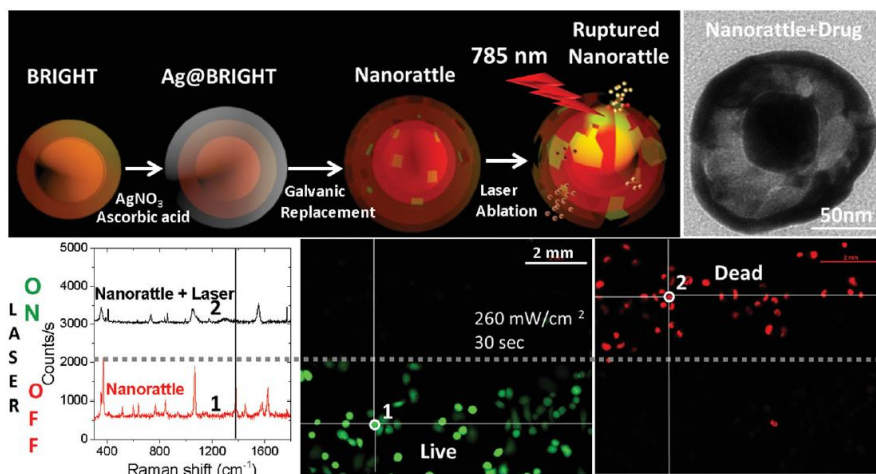

Figure 3.7 - Spectrum-guided locoregional therapy. Laser ablation of nanorattles leads to SKBR3 cell death in regions exposed to laser light, as indicated by red fluorescence. Also, the laser ablation leads to SERS signal-flip, which enables one to distinguish between live and dead cells as indicated by the Raman spectra collected from the two different regions (indicated as 1 and 2).

the nanorattles. The intact nanorattles exhibit SERS bands corresponding to NT reporters that are on the outer surface of BRIGHTs, whereas rupture of nanorattles results in appearance of SERS bands corresponding to BDT. To confirm the switch in the Raman signal, we photothermally ruptured the nanorattles using a NIR light (808 nm) as external trigger. As expected, when the nanorattles are intact, they exhibit SERS peaks corresponding to NT, which upon rupture of nanorattles disappears with concomitant appearance of BDT signal.

We employed 808 nm laser with a power density of 254 mW/cm^2 to cause rupture of the porous nanoshells to demonstrate the possibility of non-invasive monitoring of the externally-triggered drug delivery in vitro. It is important note that the combination therapy is conducted at high power density compared to drug release studies to induce the photothermal therapy and chemotherapy at the same time by laser ablation of nanorattles. The laser power required to raise the temperature of the nanorattles to about 40^{0}C and trigger a slow release of the drug from nanorattles is significantly lower compared to that required to achieve complete rupture of the nanorattles. We subjected half of the coverslips with 80% confluence of SKBR3 cells to laser irradiation and then collected Raman signals from both exposed and unexposed areas of the cells as indicated in Figure 3.7. We observed an intense NT SERS signal from the regions unexposed to laser whereas only BDT signal was observed from the exposed regions, which indicates that the nanorattles rupture and drug is released with laser irradiation (TEM images in Figure S12 Appendix C). We stained the cells with ethidium bromide solution and the fluorescence images are depicted in Figure 3.7 (live/dead), to confirm the locoregional therapy and cell killing. Fluorescence from the cells reveal that the regions of the sample exhibiting NT SERS signal correspond to live cells (green) whereas the regions exhibiting BDT signal correspond to regions of dead cells (red). Considering that SERS can be remotely excited and collected using NIR wavelengths, the approach suggested here can be a powerful tool, providing additional tools for controlled drug administration.

Chapter 4
Probing Distance-Dependent Plasmon-Enhanced Near-infrared Fluorescence Using Polyelectrolyte Multilayers as Dielectric Spacer

4.1 Abstract

Owing to their applications in biodetection and molecular bioimaging, near-infrared (NIR) fluorescent dyes are being extensively investigated. Most of the existing NIR dyes exhibit poor quantum yield, which hinders their translation to preclinical and clinical settings. Plasmonic nanostructures are known to act as tiny antennae for efficiently focusing the electromagnetic field into nanoscale volumes. The fluorescence emission from NIR dyes can be enhanced by more than a thousand times by precisely placing them in proximity to gold nanorods. We have employed polyelectrolyte multilayers fabricated using layer-by-layer assembly as dielectric spacers for precisely tuning the distance between gold nanorods and NIR dyes. The aspect ratio of the gold nanorods was tuned to match the longitudinal localized surface plasmon resonance wavelength with the absorption maximum of the NIR dye to maximize the plasmonically enhanced fluorescence. The design criteria derived from this study lays the groundwork for ultra-bright fluorescence bullets for in vitro and in vivo molecular bioimaging.

4.2 Introduction

Fluorescence is a highly promising and rapidly emerging molecular imaging modality because of the high sensitivity, amenability to targeting, use of non-ionizing radiation and non-toxic nature of the contrast agents.[62] Considering the nearly two order magnitude smaller endogenous absorption coefficient and minimal autofluorescence of tissue in the far red and near infrared (NIR) part of the electromagnetic spectrum (650-900 nm), NIR dyes are being extensively investigated for in vivo characterization of biological processes at the cellular and molecular levels. Over the past decade, there has been tremendous progress in the design and synthesis of novel NIR dyes that exhibit absorption and emission in the NIR window.[62a, 62c] However, the low quantum yield of most of these dyes limits their adoption

into routine in vivo and clinical applications.   Enhancing the brightness of NIR dyes will significantly improve the tissue imaging depth achieved with these molecular probes owing to the improved signal-to-noise ratio. In addition, the lower the excitation power required for fluorescence imaging in vivo minimizes photobleaching and photothermal damage.

Recent reports demonstrate that the quantum efficiency of NIR dyes can be substantially improved by "lightning rod effect" of plasmonic nanostructures, often termed as plasmon enhanced fluorescence (PEF).[63] The mechanism of PEF is relatively complex and it depends on intrinsic properties of plasmonic nanostructures (e.g., extinction, surface roughness) and chromophore (e.g., transition states and quantum yield), as illustrated by recent theoretical and experimental studies.[64] Although various reports experimentally demonstrate PEF, the design principles for achieving maximum fluorescence remain elusive. [64e, 64j, 64k, 65] Systematically addressing various factors that influence the magnitude of PEF is critical for the design of ultra-bright NIR imaging probes.
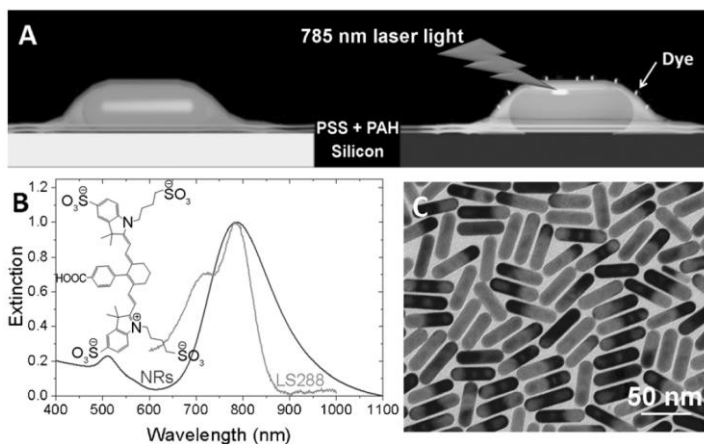
Figure 4.1 - A) Polyelectrolyte multilayers obtained by layer-by-layer assembly to precisely place the dye molecule at a desired distance from the gold nanorods. B) Vis-NIR absorption and extinction properties of LS288 and gold nanorods, respectively. The absorption maximum of the dye overlaps with extinction spectra of gold nanorods with aspect ratio 4.5, which is important to obtain maximum fluorescence enhancement. C) Representative TEM image of the gold nanorods employed in this study.

4.3 Nanorods with Polyelectrolyte Dielectric Spacers

Here, we investigate the distance-dependent fluorescence enhancement using polyelectrolyte multilayers as dielectric spacers between NIR chromophores and plasmonic nanostructures (Figure 4.1A). Polyelectrolyte multilayers of poly(allylamine hydrochloride) (PAH) and poly(styrene sulfonate) (PSS) were deposited using immersion-based layer-by-layer (LbL) assembly method as reported previously.[66] We employ a low quantum yield (0.1) NIR dye, LS288[67], as a model NIR chromophore and gold nanorods as plasmonic nanoantennae to probe the plasmon enhanced fluorescence (PEF). Gold nanorods (AuNRs) offer a distinct advantage in that the localized surface plasmon resonance (LSPR) of AuNR can be tuned over a broad range, including the NIR wavelengths, by changing the aspect ratio of AuNR.[68] The aspect ratio of the AuNR is chosen such that the longitudinal LSPR of AuNR adsorbed on glass slide overlapped with the absorption maxima of LS288 (Figure 4.1B). Representative TEM image shows AuNR with a diameter of 63±7.3 nm and a length of 14±1.7 nm, making the aspect ratio ~4.5 (Figure 4.1C).

AuNRs were chemisorbed on mercaptopropyltriethoxysilane (MPTES)-coated glass substrates. To avoid plasmon coupling, which results in broadening of the LSPR band, the density of AuNR was limited to $29\pm3/\mu m^2$ (see experimental section for details and Figure 4.3). Layer-by-layer assembly of PAH and PSS on AuNR was performed by alternate immersion of the glass substrates into 1% polyelectrolyte (PSS and PAH) solutions in 0.1 M NaCl.[66, 69] Considering that AuNRs are positively charged, we initiate the multilayer deposition with negatively charged PSS and terminate with positively charged PAH, which facilitates the electrostatic adsorption of negatively charged LS288. Deposition of
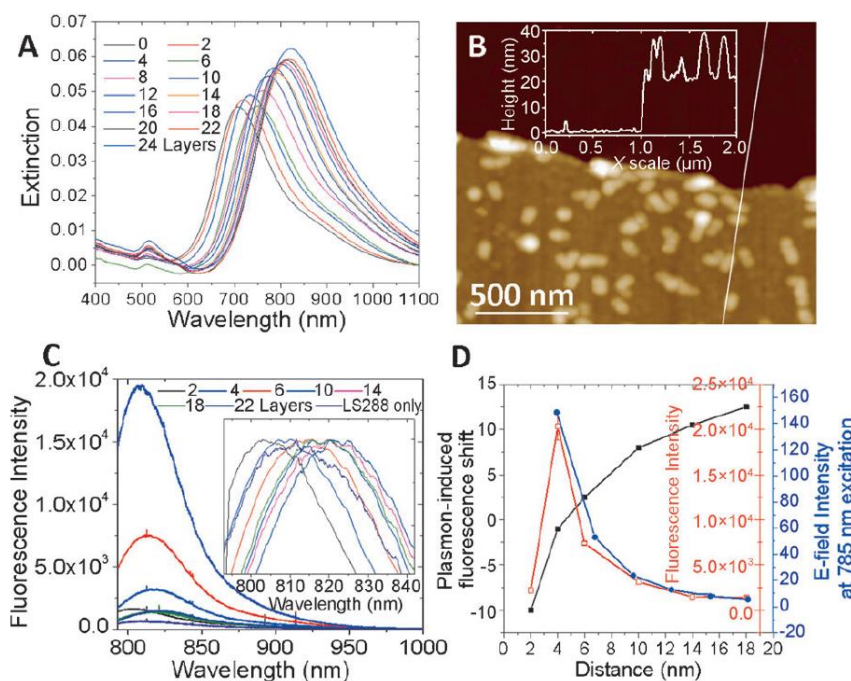

Figure 4.2 - A) Vis-NIR extinction spectra of the AuNR coated with a different number of polyelectrolyte bilayers. B) AFM image along the edge of a scratch made in a film comprised of ten polyelectrolyte bilayers. (The inset shows the cross-section across the scratch.) C) Fluorescence intensity of LS288 deposited at different distances from the AuNR surface using polyelectrolyte bilayers as spacers. D) Plot correlating the distance from the AuNR surface to the fluorescence intensity and the enhanced electromagnetic field.

polyelectrolyte layers results in a progressive red shift and increase in the intensity of longitudinal LSPR of AuNR owing to the increase in the effective refractive index of the medium around AuNR (Figure 4.2A). Atomic force microscopy (AFM) at the edge of an intentional scratch (scratch test) confirmed the thickness of the polyelectrolyte layers (Figure 4.2B and Figure S21 Appendix C). AFM height profile shows a thickness of ~20 nm after

10 bilayers of PSS and PAH, indicating an average thickness of ~1 nm for each layer (Inset in Figure 4.2B).

After the deposition of polyelectrolyte multilayers terminated with PAH, we electrostatically adsorb LS288 dye from a dilute aqueous solution (1μM) onto the polyelectrolyte surface followed by extensive rinsing to remove any weakly bound dye molecules. The uniformity of the dye adsorption on pristine glass slides was confirmed by mapping fluorescence intensity with 1 μm step-size using a confocal fluorescence microscope. All fluorescence measurements were performed using 785nm excitation at very low laser power (0.003mW) to minimize photobleaching of LS288. The fluorescence map exhibited remarkable uniformity, confirming the uniform adsorption of the fluorophores on PAH surface with no signs of patchiness (Figure S31 Appendix C). Distance-dependent PEF of LS288 was probed by adsorbing the fluorophores at different distances from AuNR surface using 2, 4, 8, 12, 16, 20, and 24 polyelectrolyte layers as spacers (Figure 4.2C). Maximum fluorescence intensity was observed for a 4 layers-spacer followed by a monotonic decrease in fluorescence intensity with increase in the number of polyelectrolyte layers (Figure 4.2 C&D). Finally, after 20 polyelectrolyte layers the fluorescence intensity equaled the intensity of dye molecules on a PAH-coated glass substrate, indicating that the fluorophores placed at ~20 nm away from the of AuNR surface are not significantly influenced by enhanced EM field of AuNR. It is worth noting that with increase in the number of bilayers the fluorescence intensity decays exponentially similar to EM field decay around the AuNR (Figure 2D). [66] These results suggest that spatial proximity of dye molecules and plasmonic nanostructures is critical to attain maximum PEF. However, when the dye molecules are in direct contact or extremely close to AuNRs (~2 nm), non-radiative energy transfer between the dye and AuNR leads to dramatic quenching of fluorescence. The optimum distance between the dye and AuNRs is found to be ~4 nm to obtain maximum fluorescence enhancement (Figure 4.2D). Therefore, if the dye is too close or too far from the AuNRs, PEF is either diminished due to non-radiative energy transfer or weak EM field, respectively.

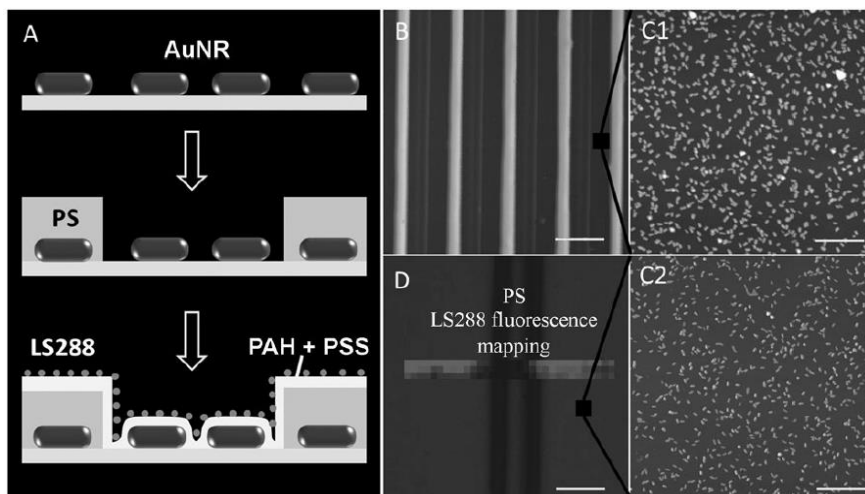# 4.4 Plasmon Enhanced Fluorescence Patterning

Figure 4.3 - A) Capillary transfer lithography to ensure large separation between a AuNR and a dye. B) AFM images of poly(styrene) (PS) stripes on a glass substrate obtained by CTL; scale bar 10 μm. AFM images of AuNRs on a glass surface between PS stripes before (C1; no layers; scale bar 1 μm) and after (C2; four layers; scale bar 1 μm) deposition of two bilayers of PSS and PAH. D) Map of the fluorescence intensity from LS288 uniformly adsorbed on AuNRs and PS following the deposition of two bilayers of PSS and PAH; scale bar 5 μm.

We have employed soft lithography to form a microscale pattern of AuNR on silicon surface to further demonstrate PEF of NIR dye in proximity to AuNR. Specifically, we employed capillary transfer lithography to form a pattern of 3 μm-wide polystyrene stripes interleaved with 7 μm-wide regions of exposed glass surface. The exposed glass surface was coated with MPTES, followed by chemisorption of AuNR (Figure 4.3B). Subsequently, two polyelectrolyte bilayers were uniformly deposited over the entire surface followed by electrostatic adsorption of LS288 as described above. Fluorescence intensity mapping across the micropattern clearly shows the enhanced fluorescence from the AuNR regions compared to that from the polystyrene regions. The enhanced fluorescence from dye molecules spaced 4 nm away from AuNR clearly demonstrates the PEF of the NIR dye (Figure 4.3D).

4.5 Coherence of LSPR and Excitation

After probing the distance-dependent PEF phenomenon, we explored the relation between the optical properties of the components (i.e., LSPR wavelength of plasmonic nanostructures and absorption and emission of the dye) and magnitude of PEF. We used gold nanorods of three different aspect ratios for this study: 1 (AuNR1), 2.3 (AuNR2.3), and 4.5 (AuNR4.5) (Figure 4.3A-C). Aspect ratio enables facile tuning of the LSPR of AuNR over a broad spectral range. In the present study, LSPR wavelength of three different AuNR is at 540 (AuNR1), 622 (AuNR2.3) and 820 nm (AuNR4.5) (Figure 4.4D).   Similar procedures described above were employed to chemisorb gold nanostructures on glass slides, deposit polyelectrolyte multilayers and electrostatically adsorb monolayer of LS288. We fixed the dielectric spacer distance at 4 nm for all the nanostructures, which was found to be optimal for maximum PEF.   We correlate the fluorescence intensities of LS288 with the extinction properties of all three nanostructures (Figure 4.4E). As expected, the PEF is primarily determined by the LSPR wavelength of the gold nanostructures. In the case of AuNR1 (i.e., gold nanospheres), the LSPR wavelength is far from the excitation and emission maxima of LS288, resulting in no significant enhancement of fluorescence. Although the extinction maximum does not completely match with absorption maximum of
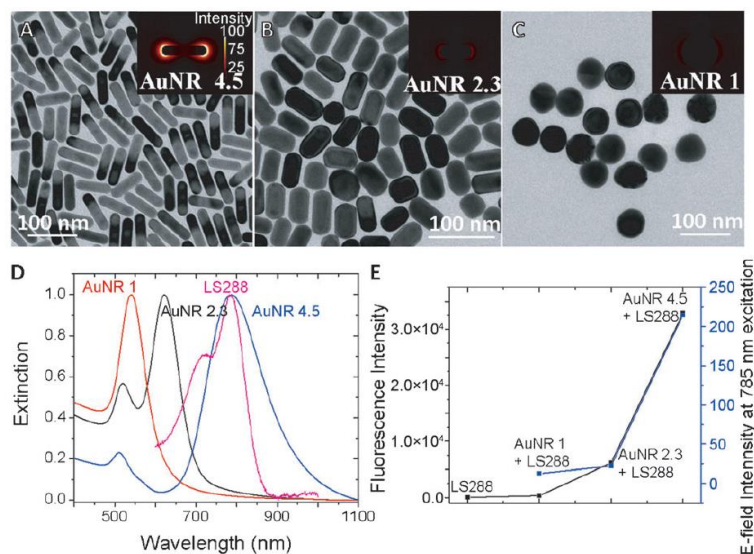

Figure 4.4 - TEM images of nanorods with aspect ratios 4.5 (A), 2.3 (B), and nanoparticles (C). D) Vis-NIR extinction spectra of AuNR 1.0, AuNR 2.3, AuNR 4.5, and LS288 (D). E) Correlation of fluorescence intensity (black) of LS288 and electric field intensity (blue) for AuNR 4.5, AuNR 2.3, and AuNR 1.0.

dye, the nanorods with an aspect ratio of 2.3 generated ~100 times higher fluorescence compared to NPs. This enhanced fluorescence is possibly due to the partial overlap of AuNRs extinction with dye absorption band. Maximum fluorescence enhancement was observed when the extinction maximum of AuNR completely matched with the absorption maximum of the dye in AuNR4.5. It is worth noting that the extinction maximum of AuNR matched with the dye emission after depositing four polyelectrolyte layers on which the dye is adsorbed.   We employed finite-difference time-domain (FDTD) simulations to estimate the EM field enhancement at the surface of these nanostructures for 785 nm excitation used in this study. FDTD simulations reveal that the electric field intensity at the surface of AuNR4.5 is nearly 8 times higher than that of AuNR2.3, which is in turn 9 times higher than that of AuNR1. Importantly, the PEF followed the same trend as the electric field intensity at the surface of these nanostructures under 785 nm excitation (Figure 4.4D-F).

While the above discussed results demonstrate the importance of spectral proximity of AuNR LSPR wavelength and absorption maximum of the NIR dye, spatial proximity of the dye molecules to AuNR is also a critical factor. To demonstrate the importance of spatial proximity, we chose AuNR with longitudinal LSPR wavelength at 670 nm, which is about 110 nm lower than the absorption maximum of the dye. After the chemisorption of AuNR on glass substrate, dye molecules were adsorbed on AuNR with 10 polyelectrolyte layers spacer. As described above, deposition of polyelectrolyte layers resulted in a red shift of the LSPR wavelength of AuNR to match the absorption maximum of the dye molecules. Although the absorption maximum of LS288 matches with the LSPR wavelength of AuNR, the fluorescence enhancement was nearly 10 times smaller than that observed for AuNR4.5 with 4 nm spacer.

Our experiments clearly reveal that the magnitude of PEF depends on the excitation wavelength, extinction and emission of dye, extinction of AuNR and distance between AuNR and dye. We can deduce the following design criteria for maximum PEF: (i) the absorption maximum of dye and extinction maxima of the metal nanostructures should have maximum overlap; (ii) the emission maximum of the dye should also partially overlap with extinction band of AuNRs; and (iii) the optimal distance (~4 nm in our study using LS288)

between dye molecules and plasmonic nanostructures is obtained by avoiding non-radiative energy transfer and ensuring strong electromagnetic field.
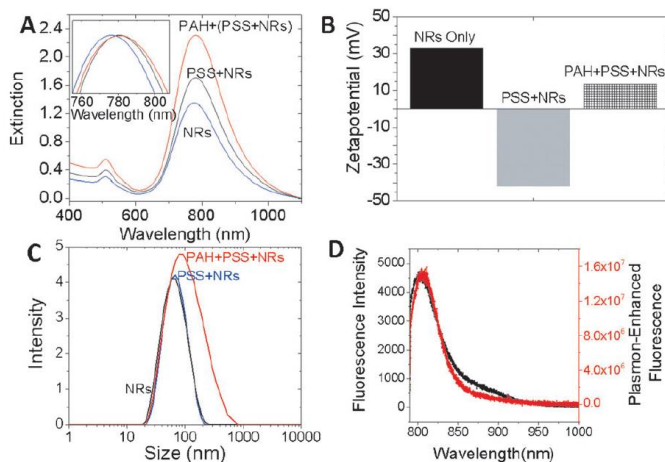

Figure 4.5 - A) Vis-NIR extinction properties of AuNR, AuNR+PSS, and AuNR+PSS+PAH. B) Zeta potential and C) dynamic light scattering of AuNR, AuNR+PSS, and AuNR+PSS+PAH further confirm the successful coating of the AuNR with polyelectrolytes. D) Comparison of the LS288 fluorescence intensity between a free dye (black) and a dye adsorbed on polyelectrolyte-coated AuNRs (red).

4.6 Plasmon Enhance Fluorescence In Solution

The design principles derived from the substrate-bound AuNR are now applied to AuNR dispersed in aqueous solution to achieve ultra-bright NIR fluorescence bullets for bioimaging applications. AuNR were coated with polyelectrolyte bilayers followed by adsorption of NIR dye at ~4nm from the surface. We confirm the charge of the polyelectrolyte layers by measuring the zeta potential of AuNR after PSS and PAH coating. The charge reversal from positive charge of pristine AuNR to negative charge upon PSS coating and subsequent reversal to positive charge with PAH coating confirm the deposition of polyelectrolyte coating on AuNR (Figure 4.5B). Dynamic light scattering (DLS) measurements reveal a 4 nm increase in hydrodynamic size after polyelectrolyte coatings, which is optimal distance between AuNR and dye for maximum fluorescence enhancement (Figure 4.5C). Fluorescence intensity from the NIR-dye adsorbed AuNR was nearly three orders of magnitude higher compared to that obtained from similar concentration of free dye in solution (Figure 4.5D).
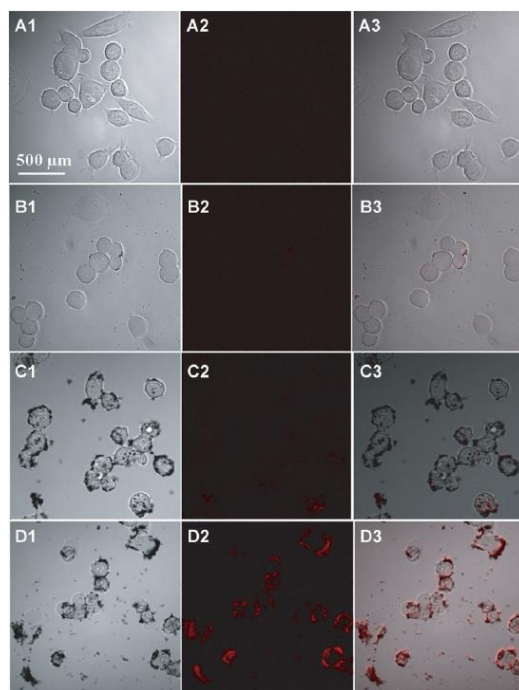
Figure 4.6 - Confocal fluorescence microscopy images of passively targeted SKBR3 cells with LS288-adsorbed AuNR 1, AuNR 2, and AuNR 4 collected using 785 nm excitation. The columns 1, 2, and 3 are bright field, fluorescence, and merged images of SKBR3 cells, respectively. The microscopy images in rows A, B, C, and D correspond to the dye alone, AuNR 1, AuNR 2, and AuNR 4.5, respectively.

4.7 Bio Imaging of PEF Probes

We demonstrate the in vitro bioimaging efficacy of the ultra-bright NIR fluorescence bullets using epithelial breast cancer cells (SKBR3). Three different nanostructures were chosen to demonstrate the bioimaging; AuNR4.5, which was found to be optimal for LS288 and AuNR2.3, and AuNR1 as controls. In all cases, the dye was adsorbed at 4 nm from the surface. SKBR3 cells were incubated with 2 ng/ml of AuNR followed by scanning confocal microscopy with 785 nm excitation. Consistent with the results discussed above, AuNR1 and AuNR2.3 exhibited low fluorescence intensity. In contrast, AuNR4.5 exhibited very bright NIR fluorescence. We have performed flow cytometry measurements of cells incubated with dye and dye-adsorbed AuNR of three different aspect ratios to further confirm the enhanced bioimaging ability. The quantification studies using flow cytometry shown in Figure 4.7 are consistent with confocal images in Figure 4.6. The fluorescence intensity from cells incubated with optimal aspect ratio AuNR (~4.5) is significantly higher

compared to dye and other AuNR samples. These results confirm that the design principles obtained from the substrate-bound AuNR could be successfully applied to achieve ultra-bright fluorescence bullets and their application for in vitro bioimaging.
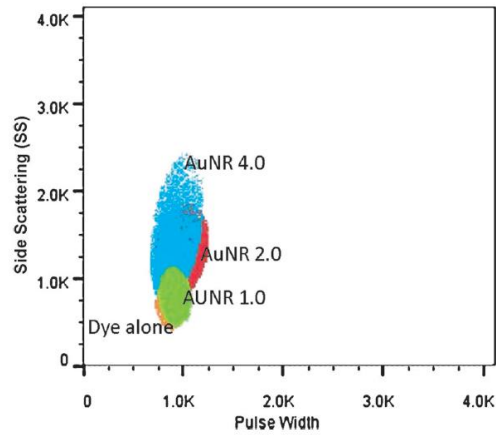

Figure 4.7 - Flow cytometry of SKBR-3 (15 000) cells incubated with a dye alone, AuNR 1.0+dye, and AuNR 2+dye, and AuNR 4+dye. Cells incubated with AuNR 4 show a significantly higher fluorescence compared to those incubated with AuNR 1.0 and AuNR 2.

Chapter 5
Conclusions

5.1 Bimetallic Nanostructures

We demonstrated that complex bimetallic Ag/Au Janus nanostructures can be achieved by a combination of kinetic control and differential surface functionalization. The proof-of-concept demonstrated here can be extended to other shape-controlled templates such as cubes and rods leading to more complex nanostructures with asymmetric composition and shape. Such fine control over the composition serves as a facile handle to finely control the optical properties of plasmonic nanostructures. Such compositionally-asymmetric nanostructures bearing synergistic properties of the components can find numerous applications in catalysis, imaging, sensing and photovoltaics.

5.2 Multifunctional Nanorattles

We then introduced a new class of multifunctional plasmonic nanostructures for locoregional combination therapy and non-invasive monitoring of the therapy process. Considering that SERS can be excited and collected in the therapeutic window (650-900 nm), the "Raman signal flip"-based monitoring of the therapy process provides additional handles for nanomedicine administration. This new class of responsive SERS probes integrated with therapeutic agents (e.g., drug delivery vehicles, photothermal contrast agents) open new possibilities in image-guided therapy, potentially replacing complex imaging systems with simple hand-held Raman devices. Furthermore, with the advent of ultrafast Raman imaging systems (e.g., StreamLine™ Plus Raman imaging), this new class of probes can potentially replace conventional live/dead staining agents such as ethidium homodimer-1 and calcein AM, which are prone to photobleaching. [61]

5.3 Plasmonic Enhanced Fluorescence

Lastly, distance-dependent enhancement of fluorescence from dye molecules adsorbed on or in close proximity to plasmonic nanoantenna is investigated using LbL assembled polyelectrolyte multilayers as dielectric spacers. A remarkable three order magnitude enhancement in fluorescence intensity was observed when the near infrared chromophores were spaced ~4 nm from the surface of gold nanorods employed as plasmonic nanoantennae. Increasing the dye-nanorod spacing resulted in a decay of plasmon enhanced fluorescence (PEF) that closely followed the decay of electric field intensity from the surface of the nanostructures. We demonstrate that significant overlap of the absorption and emission of the dye with plasmon extinction band of the plasmonic nanostructures is critical for large PEF observed here by precisely tuning the LSPR of the nanoantenna with respect to the absorption and emission of the dye. Based on the design criteria, we demonstrate ultra-bright NIR fluorescence bullets that enable significantly improved in vitro imaging of breast cancer cells. The design criteria established here can be readily extended to other NIR dyes by precise choice of plasmonic nanostructures and spacing. We expect that these findings will expedite the transition of novel NIR dyes to routine in vitro and in vivo applications.

Appendix A (Experimental Information)

Experimental (Janus Structures)

Materials

All materials were used as received without any further purification.
Cetyltrimethylammonium bromide (CTAB), gold chloride ($HAuCl_4.4H_2O$), sodium
borohydride ($NaBH_4$), ascorbic acid, 1,4-benzenedithiol (BDT), sodium chloride (NaCl),
silver nitrate ($AgNO_3$) were purchased from Sigma Aldrich (St. Louis, MO, USA).
Hydrochloric acid (HCl) was obtained from EMD (Gibbstown, NJ).
Cetyltrimethylammonium chloride (CTAC) was obtained from TCI (Portland, OR, USA).
The carbon coated copper TEM grids were acquired from Ted Pella Inc. (Redding, CA,
USA). Nanopure water (>18.0 MΩ-cm) was used for all experiments.

Characterization

TEM images were obtained using either field emission TEM (JEM-2100F, JEOL) operating
at an accelerating voltage of 200 kV or FEI sprint Lab6 with an accelerating voltage of 120
kV. UV/vis extinction spectra were collected using a Shimadzu 1800 spectrophotometer.
Raman spectra were collected using a Renishaw inVia confocal Raman spectrometer
mounted on a Leica microscope with 50× objective (NA = 0.90) in the range of 100 -3200
cm^{-1} with one accumulation and 10 sec exposure time.

Experimental (Nanorattles)

Materials

All materials were used as received without any further purification.
Cetyltrimethylammonium bromide (CTAB), gold chloride ($HAuCl_4.4H_2O$), sodium
borohydride (NaBH4), ascorbic acid, sodium chloride (NaCl), 2-naphthalenethiol (NT),
polyvinylpyrolidone (PVP (29000 MW)), 1- tetradecanol, 3-(4,5-Dimethylthiazol-2-yl)-2,5-
diphenyltetrazolium bromide (MTT) and pencillin-steptomycin were purchased from Sigma-
Aldrich (St. Louis, MO, USA). Hydrochloric acid (HCl) was obtained from EMD
(Gibbstown, NJ). Cetyltrimethylammonium chloride (CTAC) was obtained from TCI
(Portland, OR, USA). Live/Dead Viability kit (Ethidium homodimer-1 and Calcein AM) and
Trypsin-EDTA (0.25% 1X) were purchased from Life Technologies Corp. McCoy's 5A
medium and SKBR3 cell were purchased from American Type Culture Collection (ATCC).
The fromvar/carbon coated copper TEM grids were acquired from Ted Pella (Redding, CA,
USA). Nanopure water (>18.0 MΩ-cm) was used for all experiments.

Loading Dox into multifunctional nanorattles

1 mg of Dox and 25 mg of 1-tetradecanol were added to a 5 ml scintillation vial and
magnetically stirred at 90^0C. To this mixture, 100 μL of ethanol was added. Upon complete
melting of 1-tetradecanol, pre-heated Au nanorattles solution (1 ml) at 50^0C was added. The
nanorattle solution was left on the hot plate for one hour at 90^0C. After the evaporation of
ethanol, 500 μL of ice cold nanopure water was added to the mixture and the vial was set
aside to separate the Dox-loaded nanorattles. Subsequently, the nanorattles were
resuspended in water. Nanorattles were centrifuged three times at 6000 rpm for 10 minutes
to remove the excess DOX and 1-tetradecanol and redispersed in water.

Raman measurements

As synthesized BRIGHTs and nanorattles were centrifuged two times at 10,000 rpm for 10 minutes to remove the excess surfactant present in the solution and deposited on MPTES coated silicon substrate. These substrates were thoroughly rinsed with nanopure water before drying them under a stream of nitrogen to remove the unbound nanoparticles. The sparsely deposited BRIGHTs and nanorattles were identified under dark-field microscope to obtain SERS spectra of individual nanostructures.

Cell culture

Human epithelial breast cancer cells (SKBR3) were purchased from ATCC (Manassas, VA) and sub-cultured in Mc.Coy's 5A medium with 10% fetal bovine serum (FBS) and antibiotics (100 µg/ml penicillin and 100 µg/ml streptomycin) (Sigma, St. Louis, MO). Cells were grown in water jacket incubator at 37^0C with 5% CO_2-humidified atmosphere in 25 cm^2 tissue culture flasks. Once the cells reached to 90% confluence, they were washed with phosphate buffered saline (PBS) and detached with 1 mL of 0.25% trypsin-EDTA solution (Sigma). Cells were dispersed in 10 ml complete medium with 10% FBS and centrifuged. Cells were counted in trypan blue to confirm viability and plated at a density of 4×10^4 cells on poly(lysine) coated 0.5×0.5 cm^2 silicon substrates in a flat-bottom 24-well plates (Fisher Scientific, Pittsburgh, PA).

In vitro photothermal studies

The NIR irradiation using a 808 nm diode laser for various durations and power densities (63 mW/cm^2 or 260 mW/cm^2) as mentioned in the text. In the case of drug release studies, as indicated in Figure 3.3, we used substantially low laser power density (63 mW/cm^2) compared to combination therapy. Following laser treatment (260 mW/cm^2), the cells were incubated with fluorescent labels of ethidium homobromide-1 and calcein AM dyes to produce green and red emission from live and dead cells respectively, which can be visualized under fluorescence microscope.

In vitro SERS measurements of SKBR3 cells

SKBR-3 cells plated on silicon substrates were rinsed two times with PBS. Then the cells were incubated with 1 nm nanorattles for 1 hr at 37^0C. The nanorattle-incubated cells were washed three times with DPBS to remove weakly bound or non-specifically bound nanoparticles and exposed to laser at 260 mW/cm^2 power density for 1 min at specific locations. To visually identify the live and dead regions of cells, we stained the cells with commercially available live/dead cell viability reagent as described above. SERS spectra were from the dead and live cells as indicated in Figure 3.6. Raman signal is collected under confocal InVia Renishaw Raman microscope under bright field illumination and correlated with red and green fluorescence regions.

Experimental Section (Plasmon Enhanced Fluorescence)
Materials
All materials were used as received without any further purification. Polyallylamine Hydrochloride (MW: 56,000 g/mol) (PAH), Poly (sodium4-styrene sulfonate) (MW: 70,000 g/mol) (PSS), 3-(mercaptopropyl) triethoxysilane (MPTES), cetyltrimethylammonium bromide (CTAB), gold chloride ($HAuCl_4.4H_2O$), sodium borohydride ($NaBH_4$), ascorbic acid, sodium chloride (NaCl), 3-(4,5-dimethylthiazol-2-yl)-2,5-diphenyltetrazolium bromide (MTT) and pencillin-steptomycin were purchased from Sigma-Aldrich (St. Louis, MO, USA). Trypsin-EDTA (0.25% 1X) was purchased from Life Technologies Corp. McCoy's 5A medium and SKBR3 cells were purchased from American Type Culture Collection (ATCC). Hydrochloric acid (HCl) was obtained from EMD (Gibbstown, NJ). Cetyltrimethylammoniumchloride (CTAC) was obtained from TCI (Portland, OR, USA). The formvar/carbon coated copper TEM grids were acquired from Ted pella (Redding, CA, USA). Nanopure water (>18.0 MΩ-cm) was used for all experiments.

Goldnanorods adsorption on glass slides
Glass slides (1×2 cm) were cleaned using Piranha solution (3:1 sulfuric Acid to hydrogen peroxide) followed by extensive rinsing with nanopure water and drying under a stream of dry nitrogen. The Piranha-cleaned glass slides were exposed to 1% (3-mercaptopropyl) triethoxysilane in 100% pure ethanol solution for 30 minutes to render thiol functionality to glass slides. The glass slides were then rinsed with ethanol and dried under a stream of nitrogen. Subsequently, MPTES-functionalized glass slides were exposed to twice-centrifuged and acidified (pH 3) gold nanoparticle/nanorods solution for 15 min. Lowering the pH of the nanoparticle solution causes rapid adsorption of the nanoparticles onto thiol-functionalized surface. Subsequently, the glass slides were thoroughly rinsed with nanopure water to remove excess and weakly bound nanostructures. A noticeable color change of the glass slides indicates the successful adsorption of the nanostructures. UV-vis extinction spectra from glass slides exhibit distinct plasmon bands characteristic of the nanostructures adsorbed on the surface.

Polyelectrolytes coating on slides
We used a custom-made Teflon glass slide holder to deposit polyelectrolyte multilayers on glass slides. The custom-made holder minimized the handling and consequent scratching of the glass surface. This experimental setup also ensures uniformity of layer-by-layer assembly across multiple samples, while making the coating process less tedious. LbL was performed using polystyrene sulfonate (PSS) (1mM) and poly allylamine hydrochloride (PAH) (1 mM) in 100mM sodium chloride (NaCl) solution. The molarity of the solutions is calculated from the molecular weight of the monomer unit in each polymer. The weight to volume ratio for the PSS and PAH solution is 0.206 mg/mL and 0.093 mg/mL, respectively. Desired numbers of glass slides were placed in a Teflon holder and sequentially immersed in PSS, nanopure and PAH solution for 5 minutes. The process was repeated to attain desired number of polyelectrolyte multilayers. The multilayers were terminated with a PAH layer to adsorb the negatively charged NIR dye on the surface (Figure S22 Appendix C).

Polyelectrolytes coating of gold nanostructures in solution

The nanoparticles/nanorods solution was centrifuged at 8000 rpm for 12 min, which results in the formation of a pellet. The supernatant was removed and the pellet was redispersed in nanopure water. The procedure was repeated twice. To 500 μL of the nanoparticle solution, 25 μL of PSS (100 mM) was added and vortexed briefly. To the resulting mixture, 50 μL NaCl (1 mM) solution was added and vortexed briefly. The solution was subjected to magnetic stirring for 16-24 hours. Subsequently, the polyelectrolyte coated nanorods were washed by centrifugation and redispersion. The same procedure was repeated to coat the nanostructures with PAH. Desired numbers of bilayers were achieved by repeating PSS and PAH coating on the nanostructures.

Cell culture

Human epithelial breast cancer cells (SKBR3) were purchased from ATCC (Manassas, VA) and sub-cultured in Mc.Coy's 5A medium with 10% fetal bovine serum (FBS) and antibiotics (100 μg/ml penicillin and 100 μg/ml streptomycin) (Sigma, St. Louis, MO). Cells were grown in water jacket incubator at 37^0C with 5% CO_2-humidified atmosphere in 25 cm^2 tissue culture flasks. Once the cells reached to 90% confluence, they were washed with phosphate buffered saline (PBS) and detached with 1 mL of 0.25% trypsin-EDTA solution (Sigma). Cells were dispersed in 10 ml complete medium with 10% FBS and centrifuged. Cells were counted in trypan blue to confirm viability and plated at a density of $4×10^4$ cells on poly(lysine) coated 0.5×0.5 cm^2 silicon substrates in a flat-bottom 24-well plates (Fisher Scientific, Pittsburgh, PA).

Cytotoxicity Assay (MTT)

The cells were seeded at a density of $5 × 10^4$ per well in a 96-well culture plate and were incubated overnight at 37 °C with 5% CO_2. To determine the cytotoxicity of nanorattles with and without tetradecanol, seeded cells were incubated with the corresponding nanostructures for 24 hrs at 37 °C in humidified incubator with 5% CO_2. To perform MTT, the culture medium with the nanostructures was removed and replaced with the new culture medium containing MTT reagents (10%) (Sigma) followed by incubation for 4 h at 37 °C, allowing the formation of formazan crystals. The concentration of formazan crystals was measured using a plate reader by recording the UV/Vis absorption maxima at 570 nm, which represents live cells. In the case of photothermal therapy, we repeat the MTT assay at different time points to estimate the percentage of nanorattle incubated cell death before after laser exposure (Figure 23).

Fluorescence imaging

The cells were seeded on a 5 mm wide cover glass at a density of $5 × 10^4$ per well in a 24-well culture plate and were incubated overnight at 37^0C with 5% CO_2. To demonstrate the in vitro bioimaging of ultra-bright bullets, three different kinds of PEF probes as indicated in Figure 4.4 were incubated with SKBR3 cells for 4 hrs at 37^0C in humidified incubator with 5% CO_2 for passive targeting. Then the cells were fixed in 4% formaldehyde and washed three times before passivation with 1% Triton- X. Finally fixed cells were washed 3 more times in PBS buffer and image the cells with confocal fluorescence microscope at 785 nm excitation wavelength using 40X objective (Figure 6).

Fluorescence mapping procedure

All fluorescence data were collected using confocal optical microscope using 785nm laser as excitation source. A 2D map of the fluorescence intensity at 815 nm (in the case of LS288) with a 1 μm step-size is shown in Figure S13. Fluorescence map confirms the uniform adsorption of LS288 on polyelectrolyte multilayer-coated glass slide.

Instrumentation

Transmission electron microscopy (TEM) micrographs were recorded on a JEOL JEM-2100F field emission (FE) instrument. Samples were prepared by drying a drop of the solution on a carbon-coated grid, which had been previously made hydrophilic by glow discharge. The excess solution on the grid was blotted away after 30 s with filter paper. Atomic force microscopy (AFM) was performed using Dimension 3000 (Bruker) AFM in light tapping mode.[38] Triangular Si cantilevers with tip radius less than 10 nm (MikroMasch) were employed for AFM imaging. UV–vis extinction spectra were collected in air using a Shimadzu UV-1800 UV–vis spectrometer.

Appendix B
Synthesis Methods

Synthesis of nanostructures
20 nm Gold nanoparticles synthesis
Gold nanoparticles were synthesized in three steps. In the first step, seed solution was prepared by vigorous mixing of 5 ml of aqueous CTAC solution (0.2 M), 4.5 ml of nanopure water and 515 μl of $HAuCl_4$ (4.86 mM) with 450 μl of ice-cold $NaBH_4$ solution. The seed solution was aged for 1 hr at $30^{o}C$ in a hot bath. In the second step, the growth solution was prepared by mixing 4.5 ml of nanopure water, 5 ml of aqueous CTAC solution (0.2 M), 515 μl of $HAuCl_4$ (4.86 mM), and 75 μl of ascorbic acid (0.04 M). To this colorless solution, 25 μl of seed solution was added with vigorous stirring and kept undisturbed for two days to obtain highly uniform spherical nanoparticles with LSPR at 521 nm. The size of the nanoparticles obtained at this stage was 20 nm.

Core-shell structure synthesis
Au core-shell nanostructures were synthesized by employing 20 nm Au nanoparticles as cores. Prior to adding these nanoparticles to the growth solution, the nanoparticles were modified with BDT. 5 μl of BDT solution (1 mM) was added to 1 ml of 20 nm core nanoparticles (50 nM) under vigorous sonication for 10 minutes. These modified cores were centrifuged twice at 12,500 rpm for 10 minutes to remove unabsorbed BDT. Growth solution was prepared by mixing 862 μL of CTAC (0.1 M), 43 μL $HAuCl_4$ (4.86 mM), and 54 μL ascorbic acid (0.04 M). Subsequently, 43 μL of the BDT-modified cores were added to growth solution, which yields ~1 mL of Au core-shell nanostructures with BDT trapped in between the core and shell.

Core-semishell nanostructures synthesis
For synthesis of core-semishell nanostructures, Au cores were first modified with BDT. 5 μl of BDT solution (1 mM) was added to 1 ml of 20 nm core nanoparticles (50 nM) under vigorous sonication for 10 minutes. These modified cores were centrifuged twice at 12,500 rpm for 10 minutes to remove unabsorbed BDT. For forming the semishell on these BDT modified cores they were introduced into the growth solution comprised of Au precursor, ascorbic acid (reductant) and CTAC (capping agent). The growth solution was prepared by mixing 620 μL CTAC (0.1M), 31 μL $HAuCl_4$ (4.86 mM), and 39 μL ascorbic acid (1.0 M) . 310 μL of the BDT modified cores were added to this solution to yield approximately 1 mL core-semishell structures suspended in solution. The core-semishell structures were left undisturbed for three days.

Au/Ag Bimetallic core-Janus shell nanostructures
Following the synthesis of core-semishell nanostructures, exposed regions of the BDT-modified cores was passivated with PEG to facilitate preferential growth of Ag on the opposite hemisphere. For that, core-semishells were centrifuged two times at 8000 rpm to completely remove the free CTAC from the reaction and dispersed with SH-PEG solution (10 μM). The resultant solution was sonicated for 30 minutes and left on natauting mixer for 12 hours. Silver growth solution was prepared by mixing of 620 μL of CTAC (0.1 M), 31 μL of $AgNO_3$ solution (4.86 mM), and 39 μL of ascorbic acid (1.0 M). We then added 310 μL

of the PEG-passivated core-semishell nanostructures to form core-Janus shell nanostructures.

Au/Ag Bimetallic Core/Shell nanostructures

Following the synthesis of core-semishell structures as described above, the nanostructures were centrifuged and resuspended in 0.9 mM polyvinylpyrrolidone (PVP) solution followed by ultrasonication for 3-5 min. Silver growth solution was prepared by mixing 567 μL of CTAC (0.1M), 113 μL of $AgNO_3$ solution (4.86 mM), and 35 μL of ascorbic acid (1.0 M). We then added 283 μL of core-semishell structures to the silver growth solution. The particles were left undisturbed for 2-4 days.

Synthesis of multifunctional Au nanorattles

Au nanorattles were synthesized in a multistep process involving the synthesis of BRIGHTs, as described previously, followed by the formation of a porous Au shell around them. Briefly, BRIGHTs were synthesized using a method similar to seed-mediated growth, except that the cores serve as seeds in this case. 5 μl of BDT solution (1 mM) was added to 1 ml of 20 nm core nanoparticles (50 nM) under vigorous sonication for 10 minutes. These modified cores were centrifuged twice at 12,500 rpm for 10 minutes to remove unabsorbed BDT. A 20 nm thick gold shell was grown on BDT-modified cores by adding 1 ml CTAC (0.1 M), 50 μl of ascorbic acid (1 M), 50 μl of $HAuCl_4$ (4.86 mM) to 50 μl of BDT-modified core nanoparticle solution.

Following the synthesis of BRIGHTs, a silver shell was grown around these nanostructures, which was subsequently transformed into a porous gold shell using galvanic replacement reaction. For forming a silver shell on BRIGHTs, polyvinylpyrrolidone (PVP) was employed as the stabilizing agent. BRIGHTs were modified with PVP by suspending the nanostructures in 0.9 mM polyvinylpyrrolidone (PVP) solution followed by brief sonication for 3-5 minutes. Subsequently, 7.5 μL of PVP (90 mM), and 84.6 μL of ascorbic acid (1.0 M) were added to 671 μL of PVP-modified BRIGHTs. 237 μL of silver nitrate ($AgNO_3$) solution (4.86 mM) was added to the above mixture and stirred vigorously for 10 seconds. The reaction solution was left undisturbed for three to four days to allow the formation of Ag@BRIGHT nanostructures.

Galvanic replacement reaction was employed to transform the silver shell of Ag@BRIGHT into a porous gold shell. The Ag@BRIGHTs solution was centrifuged for 10 minutes at 8,000 rpm and resuspended in 1 mM PVP solution. 2 mL of the PVP-modified Ag@BRIGHTs solution was brought to boil by heating at 100℃. $HAuCl_4$ (1 mM) solution was added to the Ag@BRIGHTs at a rate of 500 μL/minute, while constantly stirring the solution. Addition of gold salt was stopped once the solution turned to vibrant blue/purple color. The volume of $HAuCl_4$ added was approximately 1.4 mL. However, the exact volume of the solution is determined by the thickness of Ag shell.

Synthesis of shape-controlled gold nanostructures

Various shape-controlled gold nanostructures were synthesized using seed-mediated approach reported in literature with small modifications. Gold nanorods were synthesized using a seed-mediated approach. Seed solution was prepared by adding 0.6 ml of an ice-cold sodium borohydride solution (10 mM) into 10 ml of 0.1 M cetyltrimethylammonium

bromide (CTAB) and 2.5×10^{-4} M chloroauric acid ($HAuCl_4$) solution under vigorous stirring at room temperature. The color of the seed solution changed from yellow to brown. Growth solution was prepared by mixing 95 ml of CTAB (0.1 M), 0.5 ml of silver nitrate (10 mM), 4.5 ml of $HAuCl_4$ (10 mM), and 0.55 ml of ascorbic acid (0.1 M) consecutively. The solution was homogenized by gentle stirring. To the resulting colorless solution, 0.12 ml of freshly prepared seed solution was added and set aside in the dark for 14 h prior to use, the AuNR solution was centrifuged twice at 10,000 rpm for 10 min to remove excess CTAB and redispersed in nanopure water (18.2 MΩ-cm). Details of other nanostructures synthesis are provided in the supporting information.

Appendix C
Supporting Information
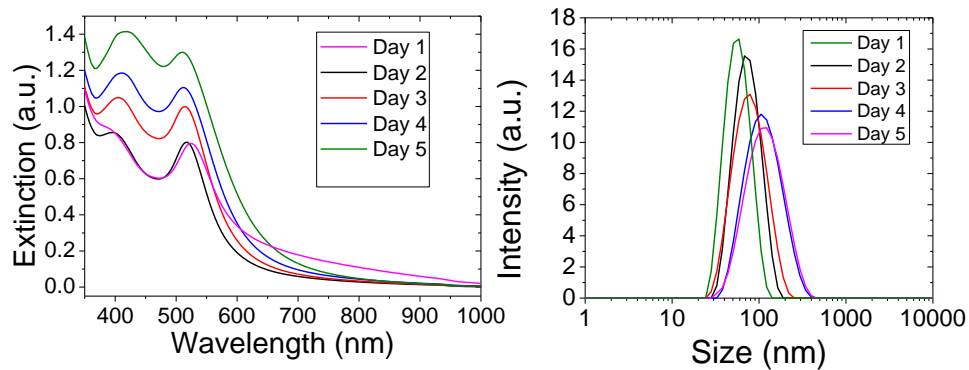
Figure S1 - UV/Vis extinction spectra of Ag@BRIGHT core/shell nanostructures at different time points of Ag growth on BRIGHTs. The thickness of the silver is crucial to tune optical properties of

Figure S2 - Ag@BRIGHTs solution in a 200 ml bottle demonstrating the feasibility of large scale synthesis of the nanostructures and the solutions in centrifuge tubes exhibit the color of BRIGHTs, Ag@BRIGHTs, and nanorattles.
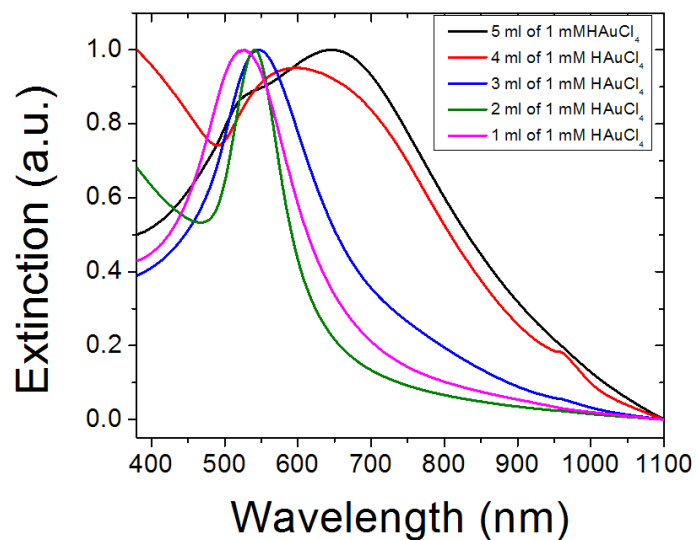
Figure S4 - UV/Vis extinction spectra of different sizes of nanorattles. The thickness of the porous shell leads to significant change in absorption in NIR region as shown above.
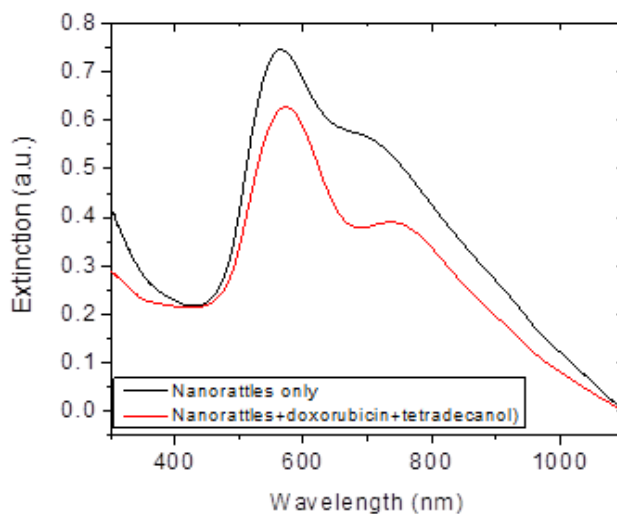
Figure S3 - Uv/Vis extinction spectra of nanorattles before and after loading phase change material, 1-tetradecanol, to contain or release the doxorubicin upon laser irradiation.
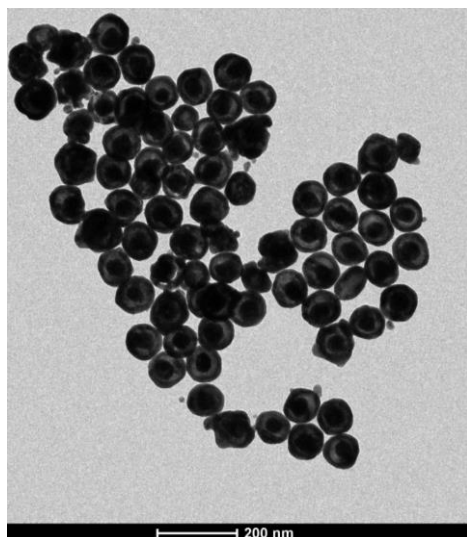
Figure S5 - TEM image of 1-tetradeconol + Dox loaded nanorattles.
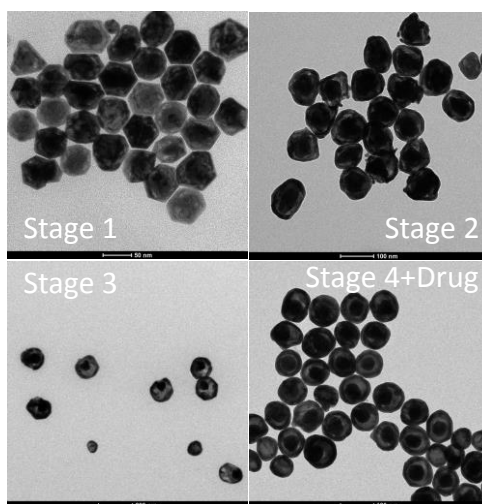
Figure S6 - TEM images of Nanorattles at different stages of Galvanic replacement of Ag@BRIGHTs
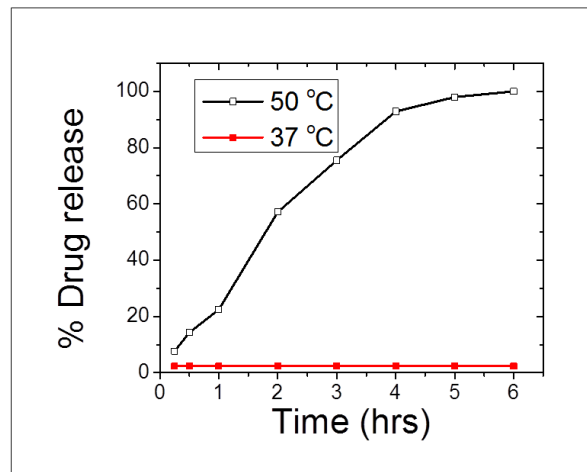
Figure S7 - Time-dependant doxorubicin release from nanorattle at 50 °C and 37 °C depicting the progressive release of Dox at 50°C and absence of release at 37 °C.
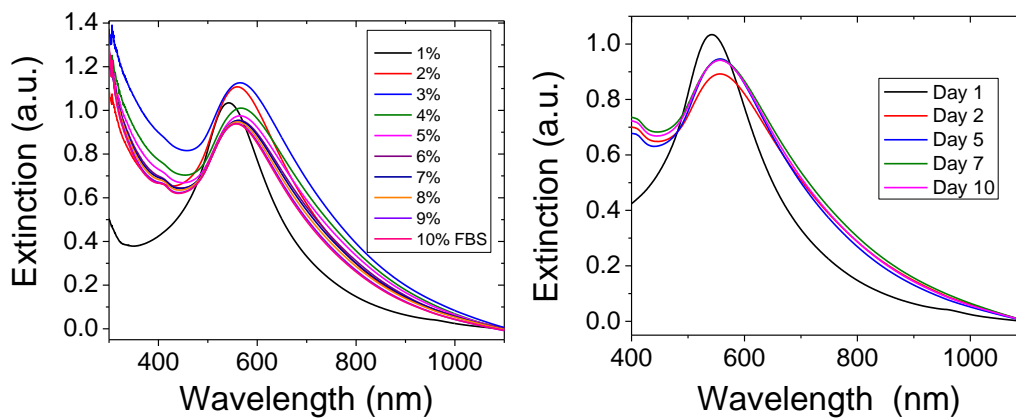
Figure S8 - Serum stability of nanorattles in (left) different percentages of FBS and (right) at different time points in 10 % FBS.
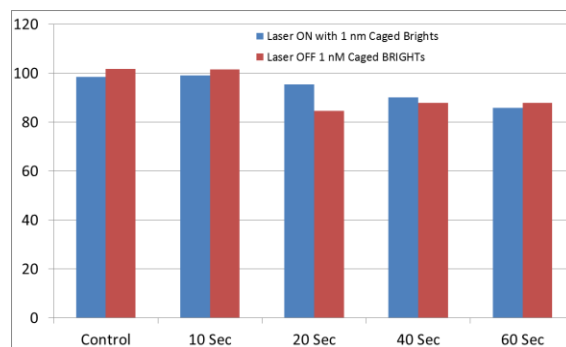
Figure S9 - Cell viability as probed by MTT assay at different laser exposure times with a power density of 63.4 mW/cm² in the presence of 1 ng/ml nanorattles.
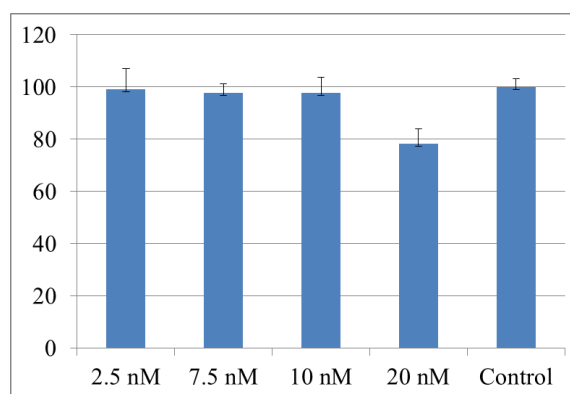
Figure S10 - Cell viability as determined by MTT assay for different concentrations of nanorattles loaded with 1-tetradeconol after laser irradiation with a power density of 63.4 mW/cm² for 30 sec.
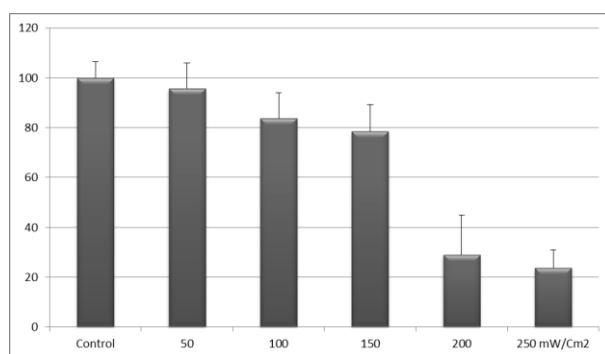
Figure S111 - Cell viability as determined by MTT assay at different laser power densities in the presence of 1ng/mL nanorattles loaded with 1-tetradecanol
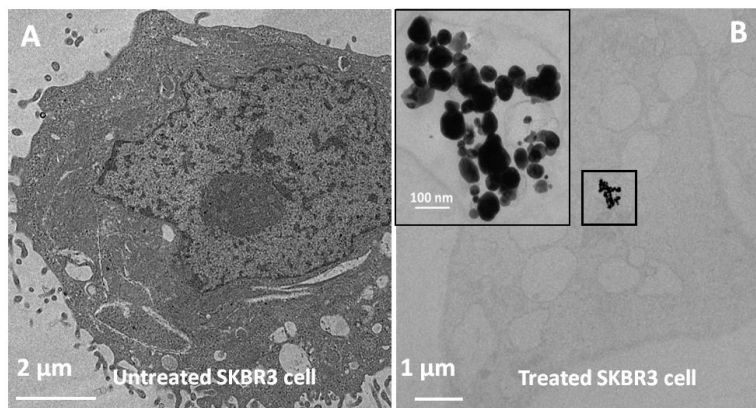
Figure S12 . Transmission electron microscopy images of sectioned SKBR3 cell before and after photothermal therapy. The inset in figure B clearly shows the ruptured nanorattles after photothermal therapy.
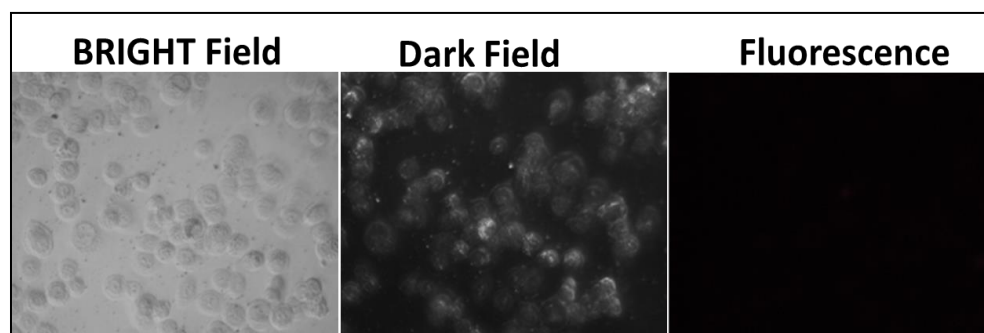
Figure 13 - *In vitro* fluorescence images of SKBR3 cells after incubation with Dox loaded Nanorattles in the absence of laser exposure.
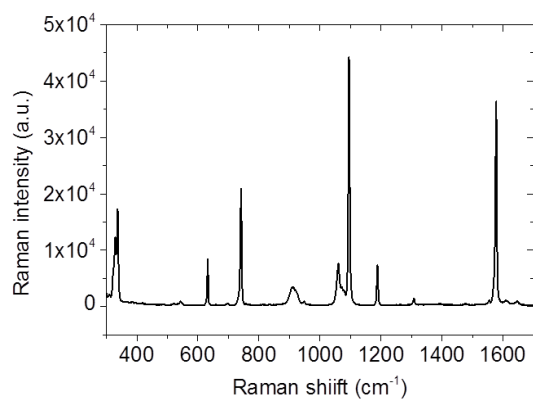
Figure S 14. Raman scattering spectrum of 1,4-benzenedithiol powder.
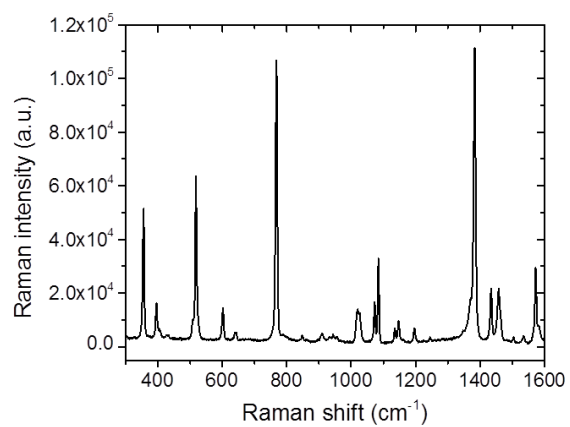
Figure S 15 – Raman scattering spectrum of 2-naphthalenethiol powder.
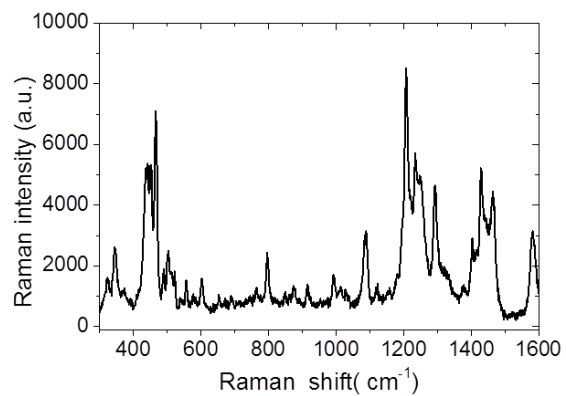
Figure S 15 - Raman scattering spectrum of doxorubicin powder.
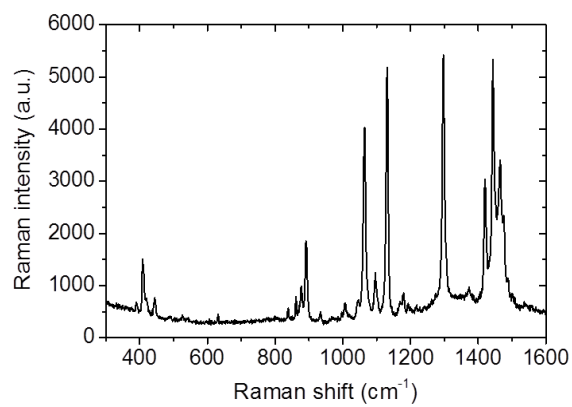
Figure S 16 - Raman scattering spectrum of 1-tetradecanol powder.
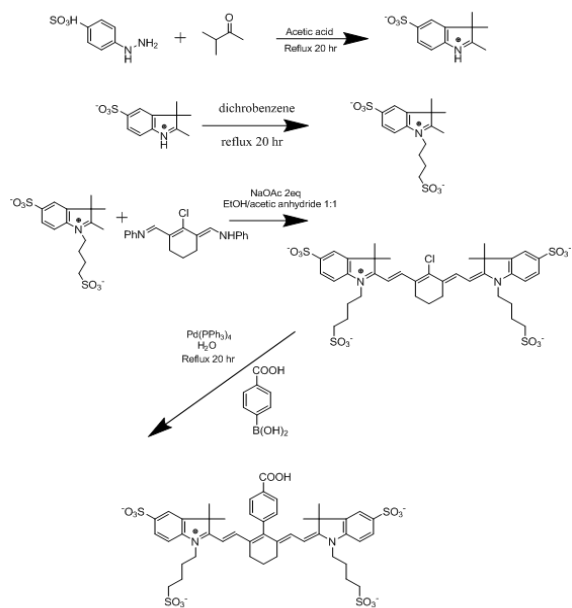
Figure S 18 - Different steps involved in the synthesis of LS288.
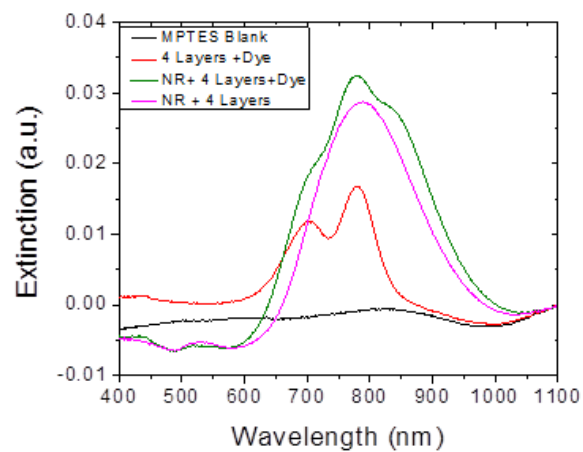
Figure S 19 - Vis-NIR extinction spectra obtained from (i) MPTES coated blank glass slides (ii) Dye adsorbed on PAH (iii) AuNR coated with two bilayers and (iv) AuNR coated with two bilayers followed by dye adsorption.
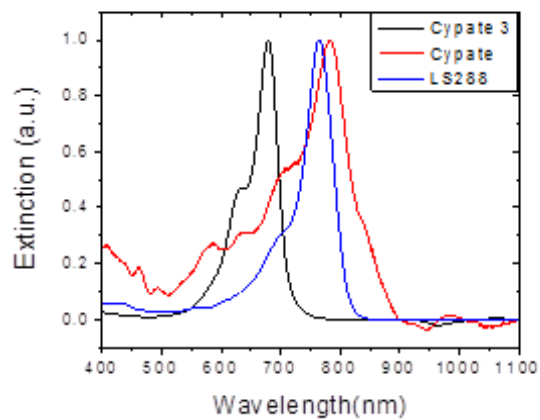
Figure S 20 - Vis-NIR extinction spectra of three different dyes: LS288, Cypate and Cypate-3

56
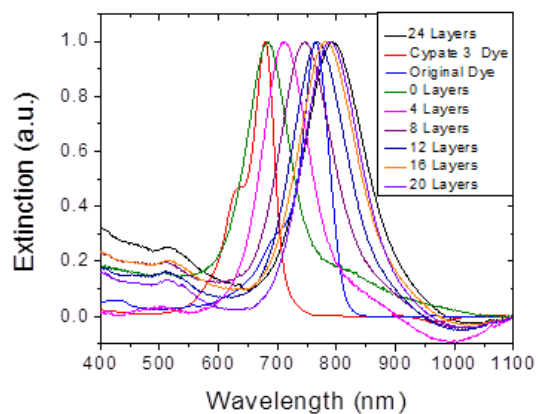
Figure S 21 - Vis-NIR extinction spectra of AuNR coated glass slides with varying number of polyelectrolyte layers compared to the peak position of the LS288 and Cypate 3 dyes
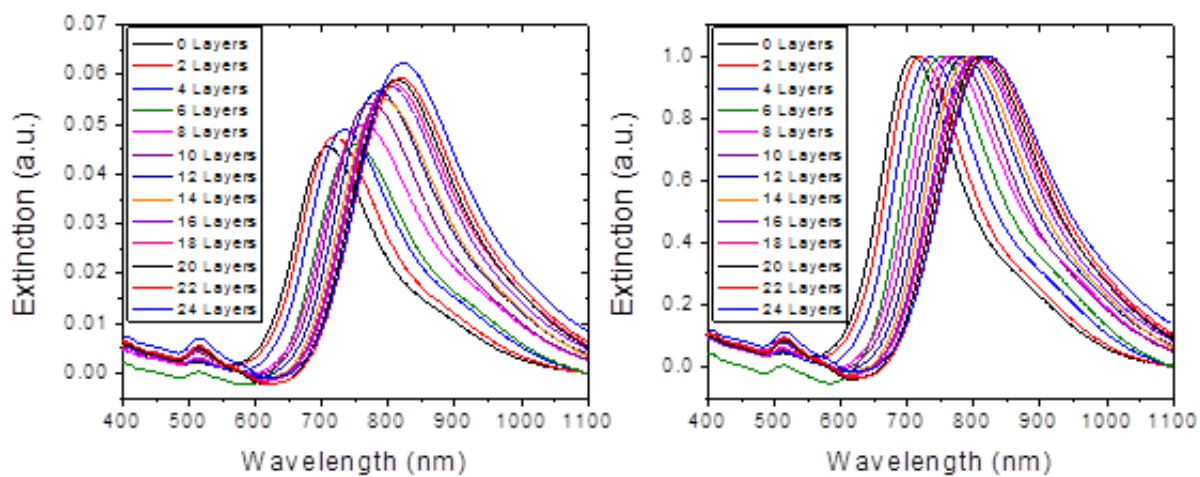

Figure S 22 - Vis-NIR extinction spectra of AuNR with PEMs after each bilayer coating. Normalized extinction spectra exhibit progressive red-shift after every bilayer due to the increase in local refractive index with polyelectrolyte coating.
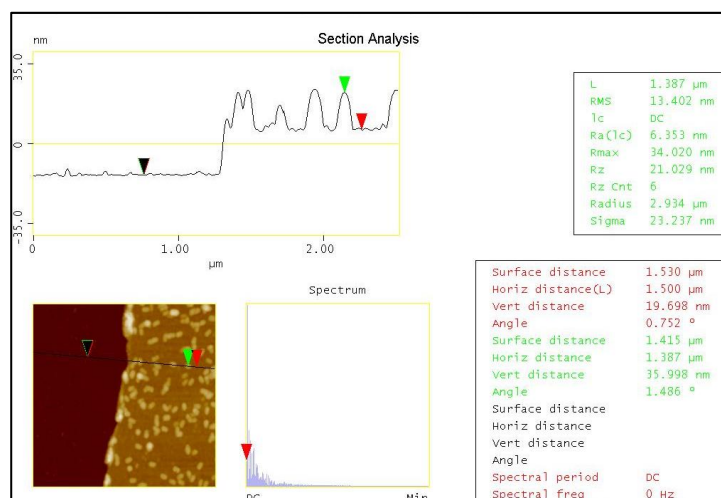
Figure S 23 - AFM analysis of gold nanorods adsorbed glass slide coated with 20 layers of PEMs.
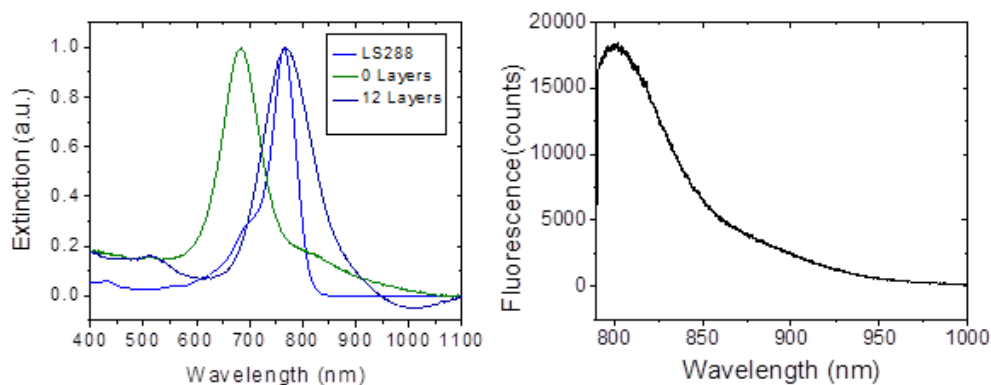

Figure S 24 - Vis-NIR extinction spectra of AuNR with 0 layers and 12 layers compared with the absorption spectrum of LS288. After the deposition of 12 layers of polyelectrolytes on AuNR the LSPR of AuNR matches with the absorption of the dye. However, the increased distance from the surface of AuNR results in smaller (nearly 5 times) PEF compared to the best case (i.e., 4 layers separation and LSPR match with absorption).
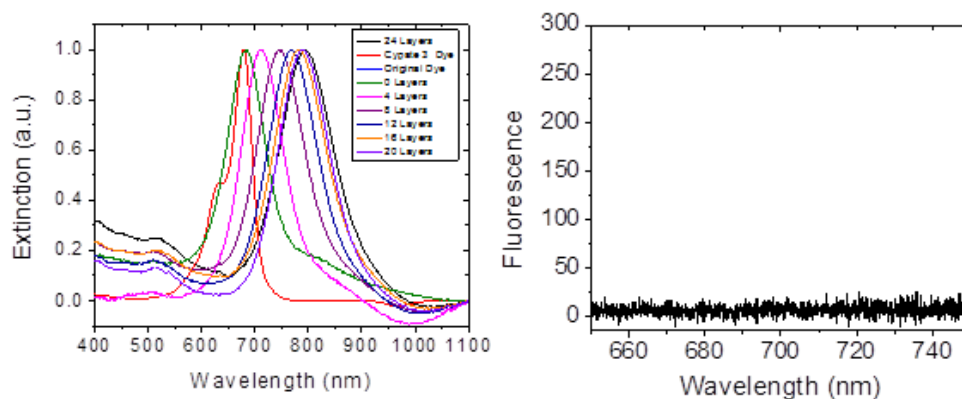
Figure S 25 - Vis-NIR extinction spectra of a control dye Cypate-3 adsorbed on AuNR. Although the LSPR of AuNRs matches with the laser excitation, no fluorescence was observed due to the mismatched absorption maximum of the dye. This indicates the importance of the overlap of the dye absorption with LSPR of the nanostructures.
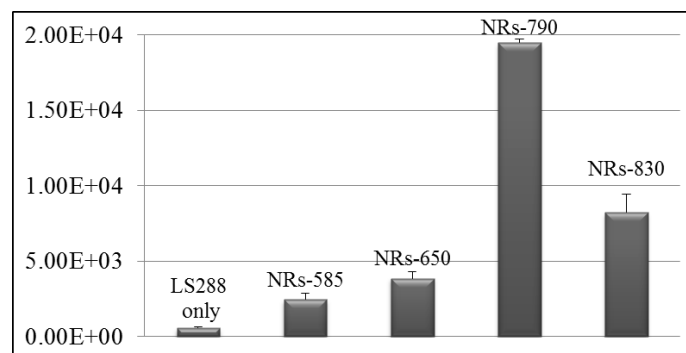

Figure S 26 - PEF of dye adsorbed on AuNR of different aspect ratio. The maximum PEF was obtained in the case of NRs-790 due to strong overlap of the LSPR of AuNR and absorption of the dye.
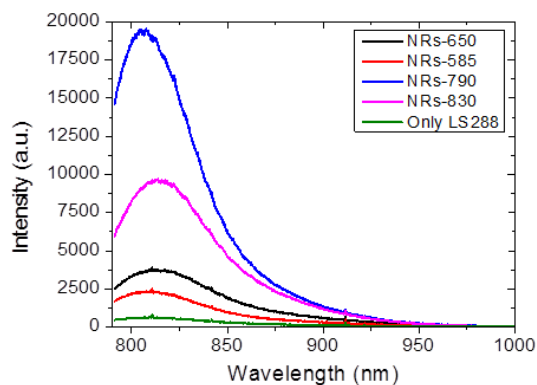
Figure S 27 - Fluorescence spectra of LS288 adsorbed on AuNR of different aspect ratio. The LSPR wavelength of AuNR is indicated in the plot.
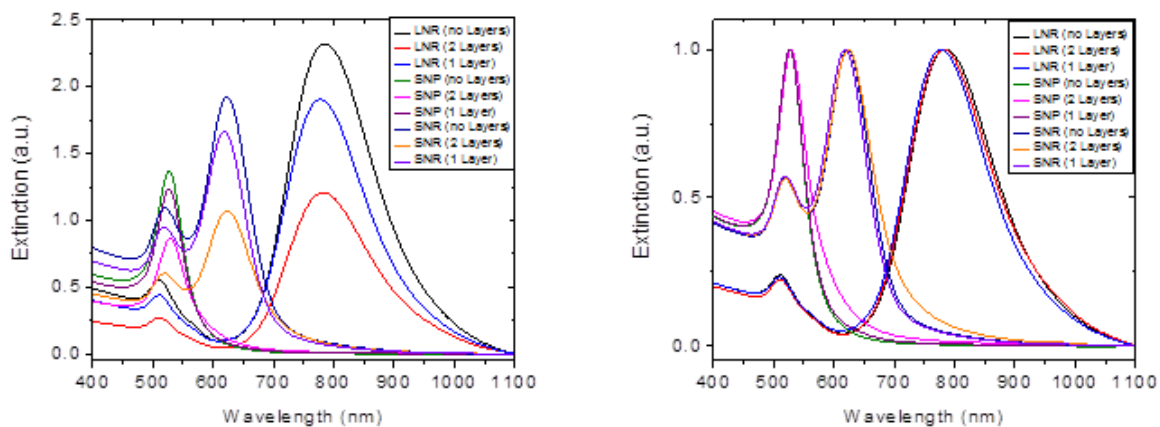

Figure S 28 - Vis-NIR extinction spectra of AuNR-4.5, AuNR-2.3, and AuNR-1 in solution before (left) and after (right) polyelectrolyte coating.

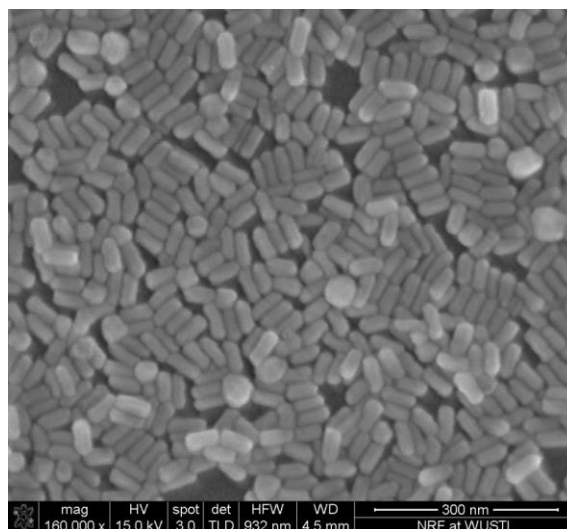**Figure S 29 - Scanning electron microscope (SEM) image of as synthesized AuNRs prior to polyelectrolyte coating.**
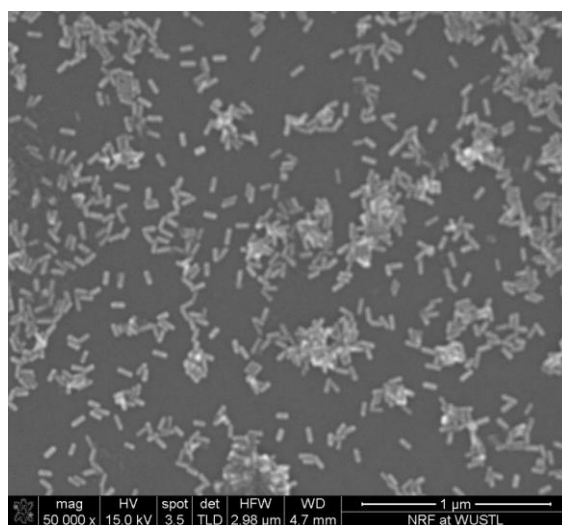
Figure S 30 - Scanning electron microscope (SEM) image of as synthesized AuNRs prior to polyelectrolyte coating.

Dimension	Average (nm)	Standard Deviation (nm)
Planet Diameter	51.40	2.35
824NR Length	62.99	7.35
824NR Width	13.91	1.73
624NR Length	44.37	5.45
624NR Width	19.93	3.09

Table S 1 - Size distribution of the nanorods and nanoparticle used in this article.
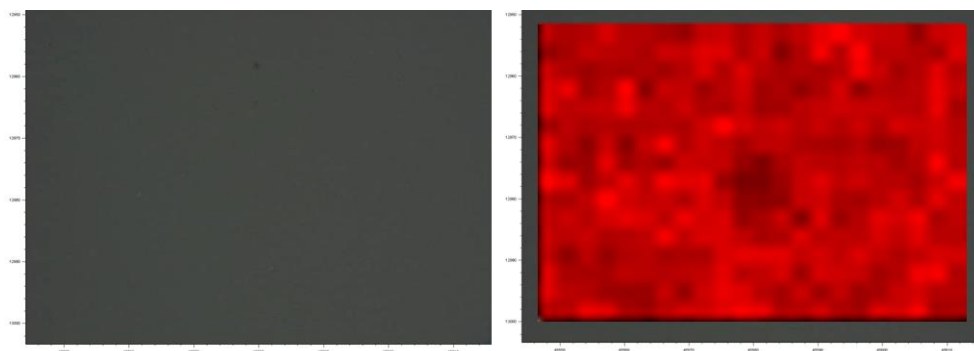
Figure S 31 - Fluorescence mapping of LS288 on PAH coated glass slide.
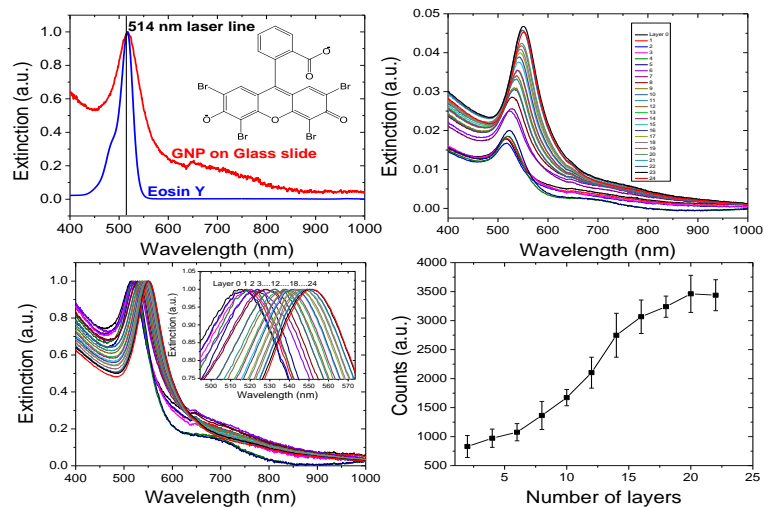
Figure S 32 - (A) Absorption spectrum of Eosin Y (Inset) and extinction properties of GNPs adsorbed on glass slide. (B) Extinction spectra of GNPs obtained after the deposition of "n" bilayers indicated in the plot. (C) Progressive red shift after polyelectrolyte layers on GNPs confirms the successful deposition of polyelectrolytes. (D) Plot depicting the increase in fluorescence intensity with increasing spacing between the Eosin Y and GNPs.

Figure S 33 - Plot depicting the LSPR shift after deposition of polyelectrolyte layers on GNPs deposited glass slide.

Figure S 34 - Atomic Force Microscopy is employed to measure the thickness of polyelectrolyte layers after 12 layers on GNPs deposited glass slide. We confirmed that the average thickness of each layer is ~ 1 nm.

References

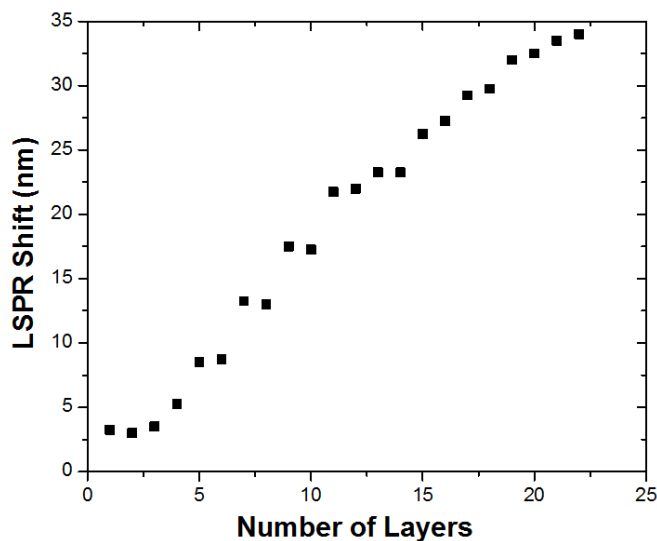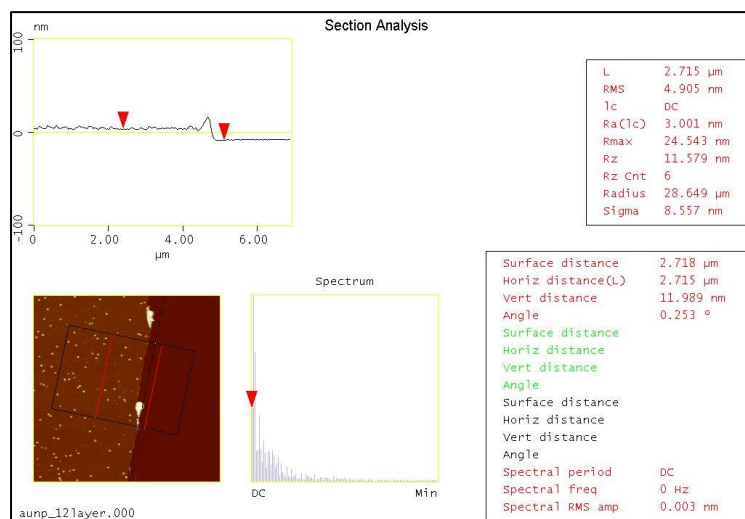[1] N. Gandra, L. Tian, S.Z. Nergiz, S. Singamaneni. Migration of plasmonics from static to dynamic. J. of Nano Science Letters. 2013. 4:23.

[2] R. Kattumenu, C.H. Lee, S. Singamaneni. Non-Spherical Metal Nanostructures and Their Assemblies for Surface Enhanced Raman Spectroscopy. American Sci. Pub. 2011. 1, 113-135.

[3] K.A. Willets, R.P. Van Duyne. Localized Surface Plasmon Resonance Spectroscopy and Sensing. Annu. Rev. Phys. Chem. 2007. 58, 267-267.

[4] Y. Xia, Y. Xiong, B. Lim, S.E. Skrabalak: Shape-Controlled Synthesis of MetalNanocrystals: Simple Chemistry Meets Complex Physics? Angew. Chem. Int. 2009. 48, 60 –103.

[5] J. Homola, Surface Plasmon Resonance Sensors for Detection of Chemical and Biological Species. Chem. Rev. 2008, 108, 462-493.

[6] J. Homola, Present and future of surface plasmon resonance biosensors. Anal. Bioanal. Chem. 2003, 377, 528-539.

[7] N.L. Rosi; C.A. Mirkin, Nanostructures in Biodiagnostics. Chem. Rev. 2005, 105, 1547-1562.

[8] B.M. Reinhard, M. Siu, H. Agarwal, A.P. Alivisatos, J. Liphardt. Calibration of Dynamic Molecular Rulers Based on Plasmon Coupling between Gold Nanoparticles. Nano Lett. 2005, 5, 2246-2252.

[9] B. Sepulveda, P.C. Angelome, L.M. Lechuga, L.M. Liz-Marzán. LSPR-based nanobiosensors. Nano Today 2009, 4, 244-251.

[10] A.J. Haes, R.P. Van Duyne. A Nanoscale Optical Biosensor: Sensitivity and Selectivity of an Approach Based on the Localized Surface Plasmon Resonance Spectroscopy of Triangular Silver Nanoparticles. J. Am. Chem. Soc. 2002, 124, 10596-10604.

[11] J.C. Riboh, A.J. Haes, A.D. McFarland, C.R. Yonzon, R.P. Van Duyne. A Nanoscale Optical Biosensor: Real Time Immunoassay and Nanoparticle Adhesion. J. Phys. Chem. B 2003, 107, 1772-1780.

[12] C.R. Yonzon, E. Jeoung, S. Zou, G.C. Schatz, M. Mrksich, R.P. Van Duyne. A Comparative Analysis of Localized and Propagating Surface Plasmon Resonance Sensors: The Binding of Concanavalin A to a Monosaccharide Functionalized Self-Assembled Monolayer. J. Am. Chem. Soc. 2004, 126, 12669-12676.

[13] A.J. Haes, L. Chang, W.L. Klein, R.P. Van Duyne. Detection of a Biomarker for Alzheimer's disease from Synthetic and Clinical Samples using a Nanoscale Optical Biosensor. J. Am. Chem. Soc. 2005, 127, 2264-2271.

[14] S.M. Nie, S.R. Emory. Probing Single Molecules and Single Nanoparticles by Surface-Enhanced Raman Scattering. Science 1997, 275, 1102–1106.

[15] K.M. Mayer, F. Hao, S. Lee, P. Nordlander, J.H. Hafner. A Single Molecule Immunoassay by Localized Surface Plasmon Resonance. Nanotechnology 2010, 21, 255503.

[16] M. Svedendahl, S. Chen, A. Dmitriev, M. Käll. Refractometric Sensing Using Propagating versus Localized Surface Plasmons: A Direct Comparison. Nano Lett. 2009, 9, 4428–4433.

[17] A.M. Mohs, M.C. Mancini, S. Singhal et al.: Hand-held Spectroscopic Device for In Vivo and Intraoperative Tumor Detection: Contrast Enhancement, Detection Sensitivity, and Tissue Penetration. Anal. Chem. 2010, 82, 9058-9065.

[18] N. Stone, M. Kerssens, G.R. Lloyd, K. Faulds, D. Graham, P. Matousek: Surface enhanced spatially offset Raman spectroscopic (SESORS) imaging - the next dimension. Chem. Sci. 2011,2, 776-780.

[19] C.L. Zavaleta. E. Garai, J.T. Liu, S. Sensarn, M.J. Mandella, D. Van de Sompel, S. Friedland, J.Van Dam, C.H. Contag, S.S. Gambhir. A Raman-based endoscopic strategy for multiplexed molecular imaging. Proc Natl Acad Sci USA. 2013, 110, E2288-97.

[20] A.F. Bagley, S. Hill, G.S. Rogers, and S.N. Bhatia: Plasmonic Photothermal Heating of Intraperitoneal Tumors through the Use of an Implanted Near-Infrared Source. ACS Nano. 2013, 7, 8089–8097

[21] D. Peer, J.M. Karp, S. Hong, O.C. Farokhzad, R. Margalit, R. Langer. Nanocarriers as an emerging platform for cancer therapy. Nature Nanotech. 2007, 2, 751–760.

[22] M.J. Sailor, J. Park. Hybrid Nanoparticles for Detection and Treatment of Cancer. Adv. Mater., 2012, 24, 3779–3802

[23] J. Kim, Y. Piao, T. Hyeon. Multifunctional nanostructured materials for multimodal imaging, and simultaneous imaging and therapy. Chem Soc. Rev., 2009, 38, 372–390.

[24] B.P. Timko, T. Dvir, D.S. Kohane. Remotely Triggerable Drug Delivery Systems. Adv. Mater, 2010, 22, 4925–4923.

[25] J. Barreto, W. Malley, M. Kubeil, B. Graham, H. Stephan, L. Spiccia. Nanomaterials: Applications in Cancer Imaging and Therapy. Adv. Mater., 2011, 23, H18–H40.

[26] R.A. Petros, J.M. DeSimone. Strategies in the design of nanoparticles for therapeutic applications. Nature Reviews. 2010, 9, 615–627.

[27] M.V. Yezhelyev, X. Gao, Y. Xing, A. Al-Hajj, S. Nie, R.M. O'Regan,. Emerging use of nanoparticles in diagnosis and treatment of breast cancer. Lancet Oncol 2006, 7, 657–667.

[28] G. Bao, S. Mitragotri, S. Tong. Multifunctional Nanoparticles for Drug Delivery and Molecular Imaging. Annu. Rev. Biomed. Eng. 2013, 15, 253-282

[29] F. Yang, C. Jin, S. Subedi, C.L. Lee, Q. Wang, Y.J. Jiang, J. Li, Y. Di, D.L. Fu. Emerging inorganic nanomaterials for pancreatic cancer diagnosis and treatment. Cancer Treat. Rev. 2012, 38, 566-579.

[30] T. Nakamura, H. Akita, Y. Yamada, H. Hatakeyama, H. Harashima. A Multifunctional Envelope-type Nanodevice for Use in Nanomedicine: Concept and Applications. Acc. Chem. Res. 2012, 45, 1113-1121.

[31] M.P. Melancon, M. Zhou, C. Li. Cancer Theranostics with Near-Infrared Light-Activatable Multimodal Nanoparticles. Acc. Chem. Res. 2011, 44, 947-956.

[32] G.A. Sotiriou. Biomedical applications of multifunctional plasmonic nanoparticles. Wiley Interdiscip Rev Nanomed Nanobiotechnol. 2013, 5, 19-30.

[33] A.M. Nystrom, K.L. Wooley. The importance of Chemistry in Creating Well-Defined Nanoscopic Embedded Therapeutics: Devices Capable of the Dual Functions of Imaging and Therapy. Acc. Chem. Res. 2011, 44, 969-978.

Bimetallic Janus nanostructures via programmed shell growth

[34] S. E. Skrabalak, L. Au, X. Li and Y. Xia, Nat. Protoc., 2007, 2, 2182-2190.

[35] N. Gandra, A. Abbas, L. Tian and S. Singamaneni, Nano Lett., 2012, 12, 2645-2651.

[36] B. Nikoobakht and M. A. El-Sayed, Chem. Mater., 2003, 15, 1957-1962.

[37] N. Gandra and S. Singamaneni, Chem. Commun., 2012, 48, 11540-11542.

[38] S. Link and M. A. El-Sayed, Int. Rev. Phys. Chem., 2000, 19, 409-453.

[39] B. Rodriguez-Gonzalez, A. Burrows, M. Watanabe, C. J. Kiely and L. M. Liz Marzan, J. Mater. Chem., 2005, 15, 1755-1759.d

[40] S. Kubo, A. Diaz, Y. Tang, T. S. Mayer, I. C. Khoo and T. E. Mallouk, Nano Lett., 2007, 7, 3418-3423.

[41] N. Gandra and S. Singamaneni, Adv. Mater., 2012, doi: 10.1002/adma.201203415.

[42] L. Lu, Z. Luo, T. Xu and L. Yu, Nano Lett., 2012.

[43] E. C. Dreaden, A. M. Alkilany, X. Huang, C. J. Murphy and M. A. El-Sayed, Chem. Soc. Rev., 2012, 41, 2740-2779.

[44] X. Liu, D. Wang and Y. Li, Nano Today, 2012, 7, 448-466.

[45] J.-H. Lee, G.-H. Kim and J.-M. Nam, J. Am. Chem. Soc., 2012, 134, 5456-5459.

[46] D.-K. Lim, K.-S. Jeon, H. M. Kim, J.-M. Nam and Y. D. Suh, Nat. Mater., 2010, 9, 60-67.

[47] C. Zhu, J. Zeng, J. Tao, M. C. Johnson, I. Schmidt-Krey, L. Blubaugh, Y. Zhu, Z. Gu and Y. Xia, J. Am. Chem. Soc., 2012, 134, 15822-15831.

[48] A.-Q. Wang, C.-M. Chang and C.-Y. Mou, J. Phys. Chem. B, 2005, 109, 18860-18867.

[49] C.-W. Yen, M.-L. Lin, A. Wang, S.-A. Chen, J.-M. Chen and C.-Y. Mou, J. Phys. Chem. C, 2009, 113, 17831-17839.

[50] D.-K. Lim, K.-S. Jeon, J.-H. Hwang, H. Kim, S. Kwon, Y. D. Suh and J.-M. Nam, Nat. Nanotechnol., 2011, 6, 452-460.

[51] S. L. Kleinman, B. Sharma, M. G. Blaber, A.-I. Henry, N. Valley, R. G. Freeman, M. J. Natan, G. C. Schatz and R. P. Van Duyne, J. Am. Chem. Soc., 2012, 135, 301-308.

Multifunctional Plasmonic Nanorattles for Spectrum-Guided Locoregional Therapy

[52] a)M. F. Kircher, A. de la Zerda, J. V. Jokerst, C. L. Zavaleta, P. J. Kempen, E. Mittra,K. Pitter, R. Huang, C. Campos, F. Habte, R. Sinclair, C. W. Brennan, I. K. Mellinghoff, E. C. Holland, S. S. Gambhir, Nat. Med. 2012, 18, 829; b)L. Tian, N. Gandra, S. Singamaneni, ACS Nano 2013, 7, 4252; c)J. Lin, S. Wang, P. Huang, Z. Wang, S. Chen, G. Niu, W. Li, J. He, D. Cui, G. Lu, X. Chen, Z. Nie, ACS Nano 2013, 7, 5320; d)N. Gandra, D.-D. Wang, Y.Zhu, C. Mao, Angew. Chem. Int. Ed. 2013, doi: 10.1002/anie.201301113; e)H. Yuan, A. M. Fales, T. Vo-Dinh, J. Am. Chem. Soc. 2012, 134, 11358; f)X. Qian, X.-H. Peng, D. O. Ansari, Q. Yin-Goen, G. Z. Chen, D. M. Shin, L. Yang, A. N. Young, M. D. Wang, S. Nie, Nat. Biotech. 2008, 26, 83.

[53] a)J. A. Barreto, W. O'Malley, M. Kubeil, B. Graham, H. Stephan, L. Spiccia, Adv. Mater. 2011, 23, H18; b)J. Kim, Y. Piao, T. Hyeon, Chem. Soc. Rev. 2009, 38, 372; c)D. Peer, J. M. Karp, S. Hong, O. C. Farokhzad, R. Margalit, R. Langer, Nat. Nanotechnol. 2007, 2, 751; d)R. A. Petros, J. M. DeSimone, Nat. Rev. Drug Discovery 2010, 9, 615; e)M. J. Sailor, J.-H. Park, Adv. Mater. 2012, 24, 3779; f)B. P. Timko, T. Dvir, D. S. Kohane, Adv. Mater. 2010, 22, 4925; g)M. V. Yezhelyev, X. Gao, Y. Xing, A. Al-Hajj, S. Nie, R. M. O'Regan, Lancet Oncol. 2006, 7, 657; h)J. Yang, J. Lee, J. Kang, S. J. Oh, H.-J. Ko, J.-H. Son, K. Lee, J.-S. Suh, Y.-M. Huh, S. Haam, Adv. Mater. 2009, 21, 4339; i)M.-R. Choi, K. J. Stanton-Maxey, J. K. Stanley,

C. S. Levin, R. Bardhan, D. Akin, S. Badve, J. Sturgis, J. P. Robinson, R. Bashir, N. J. Halas, S. E. Clare, Nano Lett. 2007, 7, 3759; j)R. Bardhan, S. Lal, A. Joshi, N. J. Halas, Acc. Chem. Res. 2011, 44, 936.

[54] a)J. Chen, D. Wang, J. Xi, L. Au, A. Siekkinen, A. Warsen, Z.-Y. Li, H. Zhang, Y. Xia, X. Li, Nano Lett. 2007, 7, 1318; b)G. D. Moon, S.-W. Choi, X. Cai, W. Li, E. C. Cho, U. Jeong, L. V. Wang, Y. Xia, J. Am. Chem. Soc. 2011, 133, 4762; c)S. E. Skrabalak, J. Chen, L. Au, X. Lu, X. Li, Y. Xia, Adv. Mater. 2007, 19, 3177; d)M. S. Yavuz, Y. Cheng, J. Chen, C. M. Cobley, Q. Zhang, M. Rycenga, J. Xie, C. Kim, K. H. Song, A. G. Schwartz, L. V. Wang, Y. Xia, Nat. Mater. 2009, 8, 935; e)S. B. Lee, Nanomedicine 2007, 2, 647.

[55] S.-W. Choi, Y. Zhang, Y. Xia, Angew. Chem. Int. Ed. 2010, 49, 7904.

[56] a)N. Gandra, S. Singamaneni, Adv. Mater. 2013, 25, 1022; b)N. Gandra, S. Singamaneni, Nanomedicine 2013, 8, 317.

[57] S. E. Skrabalak, L. Au, X. Li, Y. Xia, Nat. Protoc. 2007, 2, 2182.

[58] R. A. Alvarez-Puebla, D. S. Dos Santos Jr, R. F. Aroca, Analyst 2004, 129, 1251.

[59] M.-Y. Hua, H.-W. Yang, H.-L. Liu, R.-Y. Tsai, S.-T. Pang, K.-L. Chuang, Y.-S. Chang, T.-L. Hwang, Y.-H. Chang, H.-C. Chuang, C.-K. Chuang, Biomaterials 2011, 32, 8999.

[60] A. Lesniak, A. Salvati, M. J. Santos-Martinez, M. W. Radomski, K. A. Dawson, C. Aberg, J. Am. Chem. Soc. 2013, 135, 1438.

[61] a)J. R. Abney, B. Cutler, M. L. Fillbach, D. Axelrod, B. A. Scalettar, J. Cell. Biol. 1997, 137, 1459; b)S. M. Burrows, R. D. Reif, D. Pappas, Anal. Chim. Acta 2007, 598, 135.

Probing Distance-Dependent Plasmon-Enhanced Near-Infrared Fluorescence Using Polyelectrolyte Multilayers as Dielectric Spacers

[62] a)S. Achilefu, R. B. Dorshow, J. E. Bugaj, R. Rajagopalan, Invest. Radiol. 2000, 35, 479; b)X. Chen, P. S. Conti, R. A. Moats, Cancer Res. 2004, 64, 8009; c)S. A. Hilderbrand, R. Weissleder, Curr. Opin. Chem. Biol. 2010, 14, 71; d)S. Lee, C. Vinegoni, P. F. Feruglio, L. Fexon, R. Gorbatov, M. Pivoravov, A. Sbarbati, M. Nahrendorf, R. Weissleder, Nat. Commun. 2012, 3, 2060/1.

[63] a)F. Tam, G. P. Goodrich, B. R. Johnson, N. J. Halas, Nano Lett. 2007, 7, 496; b)R. Bardhan, N. K. Grady, J. R. Cole, A. Joshi, N. J. Halas, ACS Nano 2009, 3, 744.

[64] a)Y. S. Chi, H. R. Byon, B. S. Lee, B. Kong, H. C. Choi, I. S. Choi, Adv. Funct. Mater. 2008, 18, 3395; b)Y. Fu, J. Zhang, J. R. Lakowicz, J. Am. Chem. Soc. 2010, 132, 5540; c)K. Leong, M. T. Zin, H. Ma, M. Sarikaya, F. Huang, A. K. Y. Jen, ACS Appl. Mater. Interfaces 2010, 2, 3153; d)Y. Jiang, H.-Y. Wang, H. Wang, B.-R. Gao, Y.-w. Hao, Y. Jin, Q.-D. Chen, H.-B. Sun, J. Phys. Chem. C 2011, 115, 12636; e)K. Kang,

J. Wang, J. Jasinski, S. Achilefu, Journal of Nanobiotechnology 2011, 9, 16; f)A. M. Kern, O. J. F. Martin, Nano Lett. 2011, 11, 482; g)T. Ming, H. Chen, R. Jiang, Q. Li, J. Wang, J. Phys. Chem. lett. 2011, 3, 191; h)L. Zhao, T. Ming, H. Chen, Y. Liang, J. Wang, Nanoscale 2011, 3, 3849; i)A. M. Kern, A. J. Meixner, O. J. F. Martin, ACS Nano 2012, 6, 9828; j)J.-W. Liaw, H.-Y. Tsai, C.-H. Huang, Plasmonics 2012, 7, 543; k)M. Lisunova, M. Mahmoud, N. Holland, Z. A. Combs, M. A. El-Sayed, V. V. Tsukruk, J. Mater. Chem. 2012, 22, 16745; l)T. Zhang, G. Lu, W. Li, J. Liu, L. Hou, P. Perriat, M. Martini, O. Tillement, Q. Gong, J. Phys. Chem. C 2012, 116, 8804; m)S.-Y. Liu, L. Huang, J.-F. Li, C. Wang, Q. Li, H.-X. Xu, H.-L. Guo, Z.-M. Meng, Z. Shi, Z.-Y. Li, J. Phys. Chem.C 2013, 117, 10636.

[65] a)A. Ishida, T. Majima, Analyst 2000, 125, 535; b)E. Dulkeith, A. C. Morteani, T. Niedereichholz, T. A. Klar, J. Feldmann, S. A. Levi, F. C. J. M. van Veggel, D. N. Reinhoudt, M. Möller, D. I. Gittins, Phys. Rev. Lett. 2002, 89, 203002; c)G. Schneider, G. Decher, N. Nerambourg, R. Praho, M. H. V. Werts, M. Blanchard-Desce, Nano Lett. 2006, 6, 530; d)H. Yuan, S. Khatua, P. Zijlstra, M. Yorulmaz, M. Orrit, Angew. Chem. Int. Ed. 2013, 52, 1217.

[66] L. Tian, E. Chen, N. Gandra, A. Abbas, S. Singamaneni, Langmuir 2012, 28, 17435.

[67] H. Lee, J. C. Mason, S. Achilefu, J. Org. Chem. 2006, 71, 7862.

[68] a)B. Nikoobakht, M. A. El-Sayed, Chem. Mater. 2003, 15, 1957; b)S. E. Lohse, J. R. Eller, S. T. Sivapalan, M. R. Plews, C. J. Murphy, ACS Nano 2013, 7, 4135.

[69] O. Kedem, A. B. Tesler, A. Vaskevich, I. Rubinstein, ACS Nano 2011, 5, 748.

[70] a)H.-L. Wu, C.-H. Kuo, M. H. Huang, Langmuir 2010, 26, 12307; b)P. N. Sisco, C. J. Murphy, J. Phys. Chem. A 2009, 113, 3973.

[71] a)M. E. McConney, S. Singamaneni, V. V. Tsukruk, Polym. Rev. 2010, 50, 235; b)V. V. Tsukruk, S. Singamaneni, Wiley-VCH Verlag GmbH & Co. KGaA, 2011.

Vita

Christopher Matthew Portz

Degrees   M.S. Mechanical Engineering, May 2014
B.S. Mechanical Engineering, May 2013
B.A Physics, May 2011

Professional   Physics Students of the American Institute of Physics
Societies

Publications
"Multifunctional Plasmonic Nanorattles for Spectrum-Guided Locoregional Therapy" (Publication: Advanced Materials, 2014; Cover of Advanced Materials)

"Probing Distance-Dependent Plasmon Enhanced Near-infrared Fluorescence using Polyelectrolyte Multilayers as Dielectric Spacers" (Publication: Angewandte Chemie International Edition, 2014)

"Bimetalic Janus Nanostructures via Programmed Shell Growth" (Publication: Nanoscale, 2013)